International Journal of Solids and Structures 256 (2022) 111974

Contents lists available at ScienceDirect

International Journal of Solids and Structures

journal homepage: www.elsevier.com/locate/ijsolstr

Numerical investigation of the couplings between strain localisation processes and gas migrations in clay materials

Gilles Corman [a,*], Minh-Ngoc Vu [b], Frédéric Collin [a]

[a] Urban and Environmental Engineering Research Unit, University of Liège, Allée de la Découverte 9, 4000 Liège, Belgium
[b] Andra, Châtenay-Malabry, France

ARTICLE INFO

Keywords:
H^2M couplings
Gas migrations
Strain localisation
Second gradient model
Numerical modelling
Nuclear waste disposal

ABSTRACT

Deep geological repository is the preferred solution in many countries to manage radioactive wastes, such as in France where the Callovo-Oxfordian (COx) claystone is the candidate host rock. In such clay rock formation, the drilling of storage gallery creates an Excavation Damaged Zone (EDZ) with altered flow properties in the short term, while corrosion processes release large amounts of gas in the long term. Assessing the evolution of gas pressures in the near-field and predicting the effect of the EDZ on gas transport remains a major issue. This paper presents a second gradient two-phase flow hydro-mechanical (H^2M) model tackling the multi-physics couplings related to gas transfers and fractures development. The EDZ is reproduced by shear strain localisation bands using a microstructure enriched model with a second gradient approach. The gas migration is captured by a biphasic fluid transfer model. The impact of fracturing on the flow properties is addressed by relating the permeability and the water retention curve to mechanical strains. Using this tool, numerical modelling of a drift in the COx claystone is performed with the aim of emphasising the influence of the HM couplings on gas migrations at nuclear waste disposal scale.

1. Introduction

Since its introduction in the mid-1950s, nuclear power has become a leading source of energy providing stable and massive generation of electricity thanks to nuclear power plants. However, the nuclear fuel cycle inevitably produces high-level radioactive wastes, which are harmful to living beings and the environment over time periods much longer than the human life scale (Ausness, 1979). As a consequence, the long-term management of these wastes constitutes a major issue, which has been the object of more than 50 years of extensive research (NEA Expert Group, 1986). An international consensus dating back to the early 21st century (IAEA, 2003) has recognised the deep geological disposal (Bredehoeft et al., 1978) as one of the most promising solutions for the long-lasting storage of nuclear wastes away from the biosphere. Practically, this mode of repository consists in disposing the wastes in deep and stable geological formations and relies on the multi-barriers confinement concept (Ewing et al., 2016), which offers a combination of natural and engineered layers. Radionuclides migration is this way slowed down on a time-scale consistent with the radioactive decay period, ensuring an acceptable risk level for the residual substances reaching the surface.

To guarantee the feasibility of such a solution, it is of paramount importance to fully understand the geological barrier response throughout the system lifespan. Initially, the gallery drilling process may cause stress redistribution that triggers cracks propagation in the close vicinity of the excavated cells, especially in argillaceous rocks. This may lead to the creation of an Excavation Damaged Zone (EDZ) (Tsang et al., 2005) characterised by significant changes in the hydraulic properties (Armand et al., 2014). Then, the air ventilation required during the operation phase initiates water drainage and desaturation of the host rock which may induce extra cracking (European_Commission, 2005). Finally, the repository phase ensuing the sealing and closure of the drifts, copes with hydraulic re-saturation in the short term and with thermal (Li et al., 2007) and gaseous (Volckaert et al., 1995) processes in the long term. Since the overall barrier performance is a highly complex problem to tackle, which involves multiple coupled Thermo-Hydro-Mechanical (THM) phenomena, numerical modelling turns out to be an effective technique to perform predictions at the time-scale of the storage.

Gas migrations from the geological disposal facilities to the EDZ and the undisturbed rock formation is one of the mechanisms which requires special attention because it may potentially open preferential flow paths and affect the long-term safety function of the geological barrier (Rodwell et al., 1999). Hydrogen from the anaerobic corrosion of metallic components of the system is expected to be by far the predominant source of gas (Gallé, 2000). Given the impervious

* Corresponding author.
E-mail addresses: gilles.corman@uliege.be (G. Corman), f.collin@uliege.be (F. Collin).

https://doi.org/10.1016/j.ijsolstr.2022.111974
Received 26 November 2021; Received in revised form 1 June 2022; Accepted 12 September 2022
Available online 17 September 2022

nature of the resaturated rock, gas generation goes along with overpressurisation, suggesting different hypothetical gas transport mechanisms as a function of the pressure gradients (Marschall et al., 2005). Numerical modelling has already addressed gas issue in the context of deep geological disposal for many years now, whether it is about diffusive flow of dissolved gas (Ortiz et al., 2002), or multi-phase flow (Sentís, 2014), eventually coupled with mechanical (Gerard et al., 2008) and thermal (Yu et al., 2011) effects, and resulting in the formation of localised gas-filled pathways in the porous medium (Gerard et al., 2014).

Furthermore, significant efforts have also been taken to tackle the computational complexity behind the modelling of the EDZ. The numerous approaches elaborated over the past decades focus on the short-term (Lisjak et al., 2015) or long-term (Rutqvist et al., 2009) rock mass response, integrate a damaged-based constitutive law (Pellet et al., 2009) or include hydro-mechanical couplings (Jia et al., 2008), permeability variations (Levasseur et al., 2013), flow transfers (Charlier et al., 2013), strain localisation (Pardoen et al., 2015a) or all these aspects simultaneously (Pardoen et al., 2016). Among the several options convenient to represent rock fractures, a strain localisation approach in shear band mode is adopted in the present work (Pardoen et al., 2015a). Strain localisation, defined as the accumulation of large shear strain in limited zones is commonly observed in geomaterials prior to failure (Vardoulakis et al., 1978). This choice is thus primarily motivated by experimental evidences (Armand et al., 2014) that the fracturing process is mainly governed by shear fractures around the galleries. However, the description of strain localisation behaviour using classical finite element theories leads to a ill-posed problem, which is inherently mesh-sensitive (Pietruszczak and Mróz, 1981). Therefore, a proper regularisation of the problem is needed in order to alleviate the pathological dependence to the finite element (FE) discretisation. Among the existing techniques, the local second gradient model including an enrichment of the continuum with microstructure effects (Chambon et al., 2001a) is introduced in the following.

So far, numerical models that can properly handle strain localisation phenomena in rocks considering HM (Plassart et al., 2013; Pardoen et al., 2016) or THM (Sieffert et al., 2011; Rattez et al., 2018) couplings have already been proposed, but without considering explicitly the presence of gas. The effect of the EDZ on gas migrations has been only briefly investigated by means of a simplified model of gas pressure evolution (Autio et al., 2006) or with a coupled HM-damaged model (Xue et al., 2018). Yet in both cases, the rigorous and representative development of the EDZ is eluded. This lack of numerical modelling which combines all the aspects inherent to gas migrations in low-permeable rock materials at once has stimulated the undertaking of the present work. This contribution aims thence at extending a local second gradient approach to a multiphysical context accounting for gas pressure change in order to simultaneously capture the multi-physics couplings related to gas transfers in partially saturated clay formations and the strain localisation aspects associated with the creation of the EDZ. The proposed second gradient H^2M model (standing for two-phase flow hydro-mechanical model) is thus part of an incremental work which intends to bridge the gap between the works on a second gradient model for biphasic media (Collin et al., 2006; Pardoen et al., 2015a) on the one hand, and a two-phase fluid transfer model (Gerard et al., 2008) on the other hand. More specifically, this paper pays special attention to the modelling of HM couplings prone to occur in the EDZ and susceptible to affect the kinetics of gas transfers. These couplings take the form of an evolution of the intrinsic permeability and of the water retention behaviour of the material with strains. Practically, the novelties have been implemented in the non-linear finite element code LAGAMINE developed at the University of Liège (Charlier, 1987; Collin, 2003).

This article is organised in five main parts. After this introduction, the local second gradient H^2M model is presented in Section 2, including the balance equations and the FE formulation. In the rest of the paper, the model is applied to a practical case which lies in the context of long-lived intermediate-level waste (MAVL) storage according to the French concept (Andra, 2016). Section 3 deals with the description of the numerical simulation of a MAVL storage drift, focusing particularly on the geometry and on the evolution of the boundary conditions. Three phases are specifically simulated: the excavation of the gallery, the ventilation process when the gallery is in operation and the generation and migration of Hydrogen on the long term. In addition, the constitutive models and the related parameters used for the simulations are given in Section 4. Finally, the numerical results for the different phases of the simulations are provided and analysed in Section 5, with an emphasis on the effect of the EDZ modelling on gas flows.

2. Second gradient H^2M model

Geomaterials like host rock formations for deep geological disposal are commonly subjected to strain localisation under strong loading conditions, prior to failure of the material in localised mode. This localisation of deformation basically consists in an intense accumulation of strain into narrow thin bands, which arises once the damage threshold is reached, leading to softening of the material strength and initiation of local heterogeneities like micro-cracks or fissures. The strain localisation process can thus be seen as an instability (Lyapunov, 1892), which is now generally linked to the bifurcation theory, referring to the loss of uniqueness of a problem solution (Hill, 1958; Rice, 1976). Among the various modes proposed in the literature to study the bifurcation phenomenon (Triantafyllidis, 1980; Hill and Hutchinson, 1975), the strain localisation in shear band mode, conceptualised by Rice and co-workers (Rice, 1976), is the failure mechanism that is mainly evidenced in geomaterials (Finno et al., 1996; Desrues and Viggiani, 2004). However, it is well known that numerical modelling of such kind of localised shear zones in the framework of classical finite element methods leads to a mathematically ill-posed problem suffering of a pathological dependency to the mesh size (Pietruszczak and Mróz, 1981; De Borst and Mühlhaus, 1992). Indeed, the width of the localisation zone becomes vanishingly small with refined finite element discretisation (De Borst et al., 1993), resulting in physically inadmissible results without any energy dissipation (Bažant and Belytschko, 1985). This mesh-dependence issue can be tackled by resorting to suitable regularisation techniques that introduce an internal length scale in the problem in order to control the localised band thickness and to properly model the post-localisation behaviour. In the literature, these enhanced approaches are basically gathered in two main classes. The first one consists in the enrichment of the constitutive law. This theory includes for instance the gradient plasticity, which introduces gradient of internal variables in the constitutive model (Aifantis, 1984; Zbib and Aifantis, 1988), or (implicit Peerlings et al., 1996) non-local approaches incorporating non-local internal variables (Bazant et al., 1984; Pijaudier-Cabot and Bazant, 1987). The second theory is based on the enrichment of the continuum kinematics with microstructure effects, and finds its roots in Cosserat brothers' pioneering works (Cosserat and Cosserat, 1909), subsequently extended to the formulation of continuous media with microstructure (Toupin, 1962; Mindlin, 1964; Germain, 1973).

Among the large panel of models dealing with microstructured materials, it is here proposed to use the local second gradient model originally developed by Chambon and co-workers (Chambon et al., 1998). Initially formulated for monophasic media, this model was then extended to biphasic saturated porous media (Collin et al., 2006) and enhanced with thermal effects (Sieffert et al., 2011) and partially saturated conditions with constant gas pressure (Pardoen et al., 2015a), with specific applications to the evolution of the EDZ in the context of nuclear waste disposal (Pardoen and Collin, 2017). This coupled local second gradient model is now further enriched to take variable gas pressure into account.

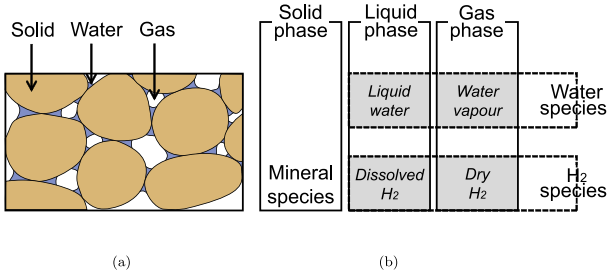

Fig. 1. (a) Unsaturated triphasic porous medium and (b) definition of phases and species.

In the presented developments, the material is treated as a porous medium commonly considered as the superposition of several continua, relying on the mixture theory (Coussy, 1995): an assembly of grains forming the solid matrix and voids between the grains filled by a combination of fluids (Fig. 1). In particular, a binary fluid mixture is considered, which includes a liquid and a gaseous phase. Each of these phases corresponds to a combination of two species, namely the liquid phase is composed of liquid water and dissolved Hydrogen while the gaseous phase is an ideal mixture of dry Hydrogen and water vapour. In the proposed formulation, it is also assumed that the mineral species and the solid phase coincide, and that solid and fluid phases are immiscible. Hereafter, the balance equations of the model are expressed, additional relationships describing solid and fluids behaviours are written and the specific 2D finite element used for the discretisation of the model is formulated.

2.1. Balance equations

Moving towards another multiphysical context accounting for gas pressure change requires an extra balance equation to capture the additional physical processes. `Lagamine` code being developed under large strains assumption, the balance equations are written in the current solid configuration for a unit volume Ω^t. Furthermore, they are expressed in the weak form following the principle of virtual work for medium with microstructure (Germain, 1973) in order to address boundary-value problems over large domains. Within this framework, microstructure effects are incorporated in the model by means of a microkinematic gradient field υ_{ij}, which defines strain and rotation at the microscale. Accordingly, additional terms are added up in the internal virtual work $W^\star_{int}$ (Germain, 1973) with respect to classical continuum mechanics, which is written as:

$$W^\star_{int} = \int_{\Omega^t} \left(\sigma^t_{ij} \frac{\partial u^\star_i}{\partial x^t_j} - \tau^t_{ij}(F^\star_{ij} - \upsilon^\star_{ij}) + \Sigma^t_{ijk} h^\star_{ijk} \right) d\Omega^t \tag{1}$$

where σ_{ij} is the Cauchy total stress field, $u^\star_i$ is the virtual displacement field, $\upsilon^\star_{ij}$ is the virtual microkinematic gradient, $F^\star_{ij}$ is the virtual macrodeformation gradient, $F^\star_{ij} - \upsilon^\star_{ij} = \bar{\varepsilon}^\star_{ij}$ is the virtual relative deformation of the microstructure, τ_{ij} is an additional stress associated to the microstructure, also called microstress, $h^\star_{ijk} = \frac{\partial \upsilon^\star_{ij}}{\partial x^t_k}$ is the virtual micro second gradient, and Σ_{ijk} is the double stress dual of $h^\star_{ijk}$, which needs an additional constitutive law introducing the internal length scale.

On the other hand, assuming that the boundary Ω^t is regular, the external virtual work $W^\star_{ext}$ reads:

$$W^\star_{ext} = \int_{\Omega^t} \rho^t_{mix} g_i u^\star_i \, d\Omega^t + \int_{\Gamma^t_\sigma} \left(\bar{t}_i u^\star_i + \overline{P}_{n,i} \upsilon^\star_{n,i} + \overline{P}_{t,ij} (\upsilon^\star_{t,ij} - \nabla_t u^\star_i) \right) d\Gamma^t \tag{2}$$

where $\rho^t_{mix} = \rho_s(1-\phi^t) + \rho^t_w S^w_r \phi^t + \rho^t_g (1 - S^w_r)\phi^t$ is the mass density of the mixture, $\phi^t = \frac{\Omega^t_v}{\Omega^t}$ is the porosity with Ω^t the current volume of a given mass of skeleton and Ω^t_v the corresponding porous volume, ρ_s is the solid grain density, ρ_w is the water density, ρ_g is the gas density, S^w_r is the water degree of saturation, g_i is the gravity, $\bar{t}_i$ is the classical external traction force per unit area, $\bar{P}_{ij}$ is an additional external double force tensor per unit area, both acting on a part Γ^t_σ of the boundary Γ of Ω^t. It is assumed that $\bar{P}_{ij}$ and $\upsilon^\star_{ij}$ can be decomposed into normal and tangential parts (Jouan et al., 2022):

$$\underline{\underline{P}} = \underline{P}_n \otimes \underline{n} + \underline{\underline{P}}_t \tag{3}$$

$$\underline{\underline{\upsilon}}^\star = \underline{\upsilon}^\star_n \otimes \underline{n} + \underline{\underline{\upsilon}}^\star_t \tag{4}$$

where,

$$\underline{P}_n = \underline{\underline{P}}.\underline{n} \quad \text{and} \quad \underline{\underline{P}}_t = \underline{\underline{P}} \circ Q_\perp \quad ; \quad \underline{\upsilon}^\star_n = \underline{\underline{\upsilon}}^\star.\underline{n} \quad \text{and}$$

$$\underline{\underline{\upsilon}}^\star_t = \underline{\underline{\upsilon}}^\star \circ Q_\perp \tag{5}$$

in which the symbol "$\circ$" denotes the composition product of two linear operators, $\underline{n}$ is the external normal at some smooth point of $\delta\Omega$ and $Q_\perp$ is the normal projection onto the tangential plane.

The local second gradient (Chambon et al., 2001a) is based on the hypothesis of equalities between the microkinematic and macrodeformation gradients, namely $\upsilon_{ij} = F_{ij} = \frac{\partial u_i}{\partial x_j}$ implying $\upsilon^\star_{ij} = F^\star_{ij} = \frac{\partial u^\star_i}{\partial x_j}$, which is introduced through a field of Lagrange multipliers λ_{ij} related to the weak form of the aforementioned constraint (Chambon et al., 1998). This finally gives the first two governing equations of the model in a weak form for every kinematically admissible virtual displacement field $u^\star_i$ and assuming $\bar{T}_i = \bar{P}_{n,i}$:

$$\begin{aligned} &\int_{\Omega^t} \left(\sigma^t_{ij} \frac{\partial u^\star_i}{\partial x^t_j} + \Sigma^t_{ijk} \frac{\partial \upsilon^\star_{ij}}{\partial x^t_k} - \lambda^t_{ij} \left(\frac{\partial u^\star_i}{\partial x^t_j} - \upsilon^\star_{ij} \right) \right) d\Omega^t \\ &\quad = \int_{\Omega^t} \rho^t_{mix} g_i u^\star_i \, d\Omega^t + \int_{\Gamma^t_\sigma} \left(\bar{t}_i u^\star_i + \bar{T}_i \upsilon^\star_{ik} n_k \right) d\Gamma^t \end{aligned} \tag{6}$$

$$\int_{\Omega^t} \lambda^\star_{ij} \left(\frac{\partial u_i}{\partial x^t_j} - \upsilon^t_{ij} \right) d\Omega^t = 0 \tag{7}$$

With a view to extending the second gradient model to multiphasic materials, the previous equations remain valid provided to define the total stress σ_{ij}. Accounting for the partially saturated conditions with Biot's definition (Biot, 1941) to consider the solid phase compressibility, the Bishop's postulate (Bishop, 1959) can be rewritten as:

$$\sigma_{ij} = \sigma'_{ij} + b_{ij}(S^w_r p_w \delta_{ij} + S^g_r p_g \delta_{ij}) \tag{8}$$

where σ'_{ij} is the Bishop's effective stress, S^w_r is the water degree of saturation, p_w and p_g are the pore water and gas pressures respectively with $s = p_g - p_w$ the matrix suction, δ_{ij} is the Kronecker symbol, and b_{ij} is Biot's tensor. In previous Eq. (8), the stress field is defined under soil mechanics convention in which compressive stress is positive.

Assuming that the double stress Σ_{ijk} is independent of water and gas pressures (second gradient effects occur solely for the solid phase) and that pore fluids have no influence at the microscale, the variations of water and gas pressures do not generate any microkinematic gradient. According to this additional assumption formulated in Ehlers and Volk

(1998), the water mass balance equation reads for every kinematically admissible virtual pore water pressure field $p_w^\star$:

$$\int_{\Omega^t} \left[\dot{M}_w^t p_w^\star + \dot{M}_v^t p_w^\star - f_{w,i}^t \frac{\partial p_w^\star}{\partial x_i^t} - f_{v,i}^t \frac{\partial p_w^\star}{\partial x_i^t} \right] d\Omega^t = \int_{\Omega^t} Q_w^t p_w^\star d\Omega^t - \int_{\Gamma_q^t} \bar{q}_w^t p_w^\star d\Gamma^t \tag{9}$$

where $f_{w,i}$ and $f_{v,i}$ are the mass flows of liquid water and water vapour respectively, $\dot{M}_w$ and $\dot{M}_v$ are the mass variations of liquid water and water vapour respectively, Q_w^t is the sink mass term of water, and Γ_q^t is the part of the boundary where the input water mass per unit area $\bar{q}_w^t$ is prescribed.

Similarly, the gas mass balance equation reads for every kinematically admissible virtual gas pressure field $p_g^\star$:

$$\int_{\Omega^t} \left[\dot{M}_{H_2}^t p_g^\star + \dot{M}_{H_2^d}^t p_g^\star - f_{H_2,i}^t \frac{\partial p_g^\star}{\partial x_i^t} - f_{H_2^d,i}^t \frac{\partial p_g^\star}{\partial x_i^t} \right] d\Omega^t = \int_{\Omega^t} Q_{H_2}^t p_g^\star d\Omega^t - \int_{\Gamma_q^t} \bar{q}_g^t p_g^\star d\Gamma^t \tag{10}$$

where $f_{H_2,i}$ and $f_{H_2^d,i}$ are the mass flows of dry Hydrogen and dissolved Hydrogen respectively, $\dot{M}_{H_2}$ and $\dot{M}_{H_2^d}$ are the mass variations of dry Hydrogen and dissolved Hydrogen respectively, $Q_{H_2}^t$ is the sink mass term of Hydrogen, and Γ_q^t is the part of the boundary where the input gas mass per unit area $\bar{q}_g^t$ is prescribed.

The fluid masses inside a porous material volume Ω are respectively equal to:

$$M_w = \rho_w \phi S_r^w \Omega \quad \text{and} \quad M_v = \rho_v \phi (1 - S_r^w) \Omega \tag{11}$$

$$M_{H_2} = \rho_{H_2} \phi (1 - S_r^w) \Omega \quad \text{and} \quad M_{H_2^d} = \rho_{H_2^d} \phi S_r^w \Omega \tag{12}$$

With respect to water and gas mass balance Eqs. (9) and (10), the time derivatives of these quantities, namely $\dot{M}_w$, $\dot{M}_v$, $\dot{M}_{H_2}$ and $\dot{M}_{H_2^d}$ must be detailed. It is performed by including the variations of liquid and gas densities of Eqs. (22), (23) and (24), by considering the porosity variation of Eq. (25) and by assuming a unit mixture volume Ω.

Moreover, the description of the fluid transport processes in partially saturated porous media relies on a biphasic flow model. As stated above, this two-phase flow model consists of a liquid phase made up of liquid water and dissolved Hydrogen and a gaseous phase, corresponding to an ideal mixture of dry Hydrogen and water vapour. Thus, the mass flows included in fluid mass balance Eqs. (9) and (10) take into account the advection of each phase using the generalised Darcy's law (Darcy, 1856) and the diffusion of the components within each phase by Fick's law (Fick, 1855), as follows:

$$f_{w,i} = \rho_w q_{l,i} \quad \text{and} \quad f_{v,i} = \rho_v q_{g,i} + i_{v,i} \tag{13}$$

$$f_{H_2,i} = \rho_{H_2} q_{g,i} + i_{H_2,i} \quad \text{and} \quad f_{H_2^d,i} = \rho_{H_2^d} q_{l,i} + i_{H_2^d,i} \tag{14}$$

where ρ_w, ρ_v, ρ_{H_2} and $\rho_{H_2^d}$ are the densities of liquid water, water vapour, dry Hydrogen and dissolved Hydrogen respectively, $q_{l,i}$ and $q_{g,i}$ are the advective fluxes respectively of the liquid and the gaseous phases, $i_{v,i}$, $i_{H_2,i}$ and $i_{H_2^d,i}$ are the diffusion fluxes respectively for the water vapour, the dry Hydrogen, and the dissolved Hydrogen. It is worth noted that the liquid water diffusion within the liquid phase is neglected in the model due to the small amount of dissolved Hydrogen in this phase.

The advection of liquid and gaseous phases is described by the generalised Darcy's law for unsaturated cases and reads:

$$q_{l,i} = q_{w,i} = -\frac{k_{ij}^{int} k_r^w}{\mu_w} \left(\frac{\partial p_w}{\partial x_j} + \rho_w g_j \right) \tag{15}$$

$$q_{g,i} = -\frac{k_{ij}^{int} k_r^g}{\mu_g} \left(\frac{\partial p_g}{\partial x_j} + \rho_g g_j \right) \tag{16}$$

where k_{ij}^{int} is the water permeability tensor in saturated conditions, i.e. the intrinsic permeability tensor, k_r^w and k_r^g are the water and gas relative permeabilities dependent on the degree of saturation, μ_w and μ_g are the dynamic viscosities of water and gaseous mixture respectively, the latter being dependent on the dynamic viscosity of each component of the mixture as:

$$\mu_g = \frac{1}{\frac{\rho_{H_2}}{\rho_g \mu_{H_2}} + \frac{\rho_v}{\rho_g \mu_v}} \tag{17}$$

The diffusion of the components within each phase is defined by Fick's law and reads:

$$i_{v,i} = -\phi (1 - S_r^w) \bar{\tau} D_{v/H_2} \rho_g \frac{\partial}{\partial x_i} \left(\frac{\rho_v}{\rho_g} \right) = -i_{H_2,i} \tag{18}$$

$$i_{H_2^d,i} = -\phi S_r^w \bar{\tau} D_{H_2^d/w} \rho_w \frac{\partial}{\partial x_i} \left(\frac{\rho_{H_2^d}}{\rho_w} \right) \tag{19}$$

where D_{v/H_2} and $D_{H_2^d/w}$ are the diffusion coefficients respectively in the gaseous mixture (dry Hydrogen–water vapour) and for the dissolved Hydrogen in liquid water, and $\bar{\tau}$ is the tortuosity of the porous medium, which characterises the path followed by the dissolved Hydrogen particles between the solid grains.

2.2. Solid and fluids phases behaviour

In order to fully describe the behaviour of the multiphasic porous medium and to solve the problem described in the previous section, the behaviour of solid and fluids phases must be further specified.

The Biot tensor introduced in Eq. (8) represents more particularly the compressibility of the solid grain skeleton relative to the skeleton compressibility, expressed in orthotropic axes as (Cheng, 1997):

$$b_{ij} = \delta_{ij} - \frac{C_{ijkl}^e}{3K_s} \tag{20}$$

where δ_{ij} is the Kronecker symbol, K_s is the isotropic bulk modulus of the solid grains, and C_{ijkl}^e is the elastic stiffness tensor of the material. It is worth noting that including the plastic material behaviour in case the medium is not assumed elastic requires an extension to poroplasticity, as proposed by Coussy (1995). Yet, these developments are not included in the present work.

On top of that, the isotropic variation of solid density is linked to the variations of pore water pressure, gas pressure and mean effective stress according to (Detournay and Cheng, 1993):

$$\frac{\dot{\rho}_s}{\rho_s} = \frac{(b_{ij} - \phi)(S_r^w \dot{p}_w + S_r^g \dot{p}_g) + \dot{\sigma}'}{(1 - \phi) K_s} \tag{21}$$

where ρ_s is the solid grain density, ϕ is the porosity and σ' is Bishop's mean effective stress.

As for the fluid phase behaviour, the fluids are assumed to be compressible which implies variations of liquid and gas densities. The isotropic compressibility of water is assumed to respect the following relationship (Lewis and Schrefler, 2000), which predicts an increase in water density as a function of water pressure:

$$\frac{\dot{\rho}_w}{\rho_w} = \frac{\dot{p}_w}{\chi_w} \tag{22}$$

where $\frac{1}{\chi_w}$ is the water compressibility.

For the gaseous mixture of dry Hydrogen and water vapour, the ideal gas law is assumed. The state equations of ideal gas (Clapeyron, 1834) and Dalton's law (Dalton, 1802) applied to dry Hydrogen and water vapour yield:

$$p_{H_2} = \frac{RT}{m_{H_2}} \rho_{H_2} \quad \text{and} \quad p_v = \frac{RT}{m_v} \rho_v \tag{23}$$

$$p_g = p_{H_2} + p_v \qquad \text{and} \qquad \rho_g = \rho_{H_2} + \rho_v \tag{24}$$

where p_{H_2} and p_v are the partial pressures of Hydrogen and vapour respectively, m_{H_2} and m_v are the molar masses of dry Hydrogen and water vapour respectively, R is the universal gas constant and T is the absolute temperature.

From the thermodynamic framework proposed in Coussy (2004), the expression of the porosity variation reads:

$$\dot{\phi} = (b-\phi)\left[\frac{S_r^w}{K_s}\dot{p}_w + \frac{1-S_r^w}{K_s}\dot{p}_g + \frac{\dot{\Omega}}{\Omega}\right] \tag{25}$$

where $\frac{\dot{\Omega}}{\Omega} = \dot{\varepsilon}_v$ is the time variation of the skeleton volumetric strain. This last Eq. (25) is basically required for the computation of the storage terms in the fluid balance Eqs. (9) and (10), introducing a coupling term between the mechanical behaviour and the fluid transfers.

2.3. Finite element formulation

The local second gradient model for multiphasic medium detailed here hinges on a series of balance Eqs. (6), (7), (9) and (10) expressed in a weak form in order to be implemented in a finite element code. Solving the loading process of a boundary-value problem consists in determining the unknown fields $(u_i, p_w, p_g, \nu_{ij}, \lambda_{ij})$ for which these equilibrium equations are valid. The numerical implementation of these equations requires the linearisation of the system of equations, with the main steps available in Appendix. Formulating the governing equations of the resulting linear auxiliary problem in matrix form helps defining the stiffness (tangent) matrix:

$$\int_{\Omega^t} \left[U^{\star,t}_{(x,y)}\right]^T \left[E^t\right] \left[dU^t_{(x_1,x_2)}\right] d\Omega^t = -\Delta_1^t - \Delta_2^t - \Delta_3^t - \Delta_4^t \tag{26}$$

where $\left[U^{\star,t}_{(x,y)}\right]$ is the vector of the unknown increments of nodal variables, $\left[dU^t_{(x_1,x_2)}\right]$ is a vector having the same structure with the corresponding virtual quantities and $\left[E^t\right]$ is the stiffness matrix storing the different terms of the coupled problem, which reads:

$$\left[E^t\right] = \begin{bmatrix} E^t_{MM} & E^t_{WM} & E^t_{GM} & E^t_{\nu M} & E^t_{\lambda M} \\ E^t_{MW} & E^t_{WW} & E^t_{GW} & E^t_{\nu W} & E^t_{\lambda W} \\ E^t_{MG} & E^t_{WG} & E^t_{GG} & E^t_{\nu G} & E^t_{\lambda G} \\ E^t_{M\nu} & E^t_{W\nu} & E^t_{G\nu} & E^t_{\nu\nu} & E^t_{\lambda\nu} \\ E^t_{M\lambda} & E^t_{W\lambda} & E^t_{G\lambda} & E^t_{\nu\lambda} & E^t_{\lambda\lambda} \end{bmatrix} \tag{27}$$

where the matrices $[E^t_{MM}]$, $[E^t_{WW}]$, $[E^t_{GG}]$ are the classical stiffness matrices for mechanical, water flow and gas flow problems, while the off-diagonal matrices contain the multi-physical coupling terms. With a view to addressing the impact of fracturing on the rock transport properties, the stiffness matrices capturing the influence of mechanics on the fluids is of particular interest in the present study and are thus specifically detailed below. The derivation of the other submatrices can be found in Chambon and Moullet (2004) for a monophasic medium further extended in Sieffert et al. (2014) to account for a multiphasic system.

$$\left[E^t_{MW}\right] = \left[\begin{array}{c|c|c|c} A^{w,t}_{111} + L^{w,t}_j + N^{w,t}_1 & A^{w,t}_{121} + N^{w,t}_1 + F^{w,t}_2 & A^{w,t}_{112} + N^{w,t}_2 & A^{w,t}_{122} + L^{w,t}_j + N^{w,t}_2 - F^{w,t}_1 \\ \hline A^{w,t}_{211} + L^{w,t}_j + N^{w,t}_1 - F^{w,t}_2 & A^{w,t}_{221} + N^{w,t}_1 & A^{w,t}_{212} + N^{w,t}_2 + F^{w,t}_1 & A^{w,t}_{222} + L^{w,t}_j + N^{w,t}_2 \\ \hline C^{w,t} + M^{w,t} & 0 & 0 & C^{w,t} + M^{w,t} \end{array}\right] + \left[K^{w,t}\right] \tag{28}$$

$$\left[E^t_{MG}\right] = \left[\begin{array}{c|c|c|c} A^{g,t}_{111} + L^{g,t}_j + N^{g,t}_1 & A^{g,t}_{121} + N^{g,t}_1 + F^{g,t}_2 & A^{g,t}_{112} + N^{g,t}_2 + N^{w,t}_2 & A^{g,t}_{122} - F^{g,t}_1 - L^{w,t}_j + L^{g,t}_j - N^{w,t}_2 + N^{g,t}_2 \\ \hline A^{w,t}_{211} - F^{g,t}_2 - L^{w,t}_j + L^{g,t}_j - N^{w,t}_1 + N^{g,t}_1 & A^{w,t}_{221} + N^{g,t}_1 - N^{w,t}_1 & A^{w,t}_{212} + N^{g,t}_2 - N^{w,t}_2 + F^{g,t}_1 & A^{w,t}_{222} + L^{g,t}_j - L^{w,t}_j + N^{g,t}_2 - N^{w,t}_2 \\ \hline C^{g,t} + M^{g,t} & 0 & 0 & C^{g,t} + M^{g,t} \end{array}\right] + \left[K^{g,t}\right] \tag{29}$$

where:

$$A^{w,t}_{ijk} = -\rho^t_w \frac{k^{w,t}_r}{\mu_w} k^{int}_{ij} \frac{\partial p^t_w}{\partial x^t_k} - \rho^t_v \frac{k^{g,t}_r}{\mu_g} k^{int}_{ij} \frac{\partial p^t_g}{\partial x^t_k}$$
$$\text{and} \qquad A^{g,t}_{ijk} = -\rho^t_{H_2} \frac{k^{g,t}_r}{\mu_g} k^{int}_{ij} \frac{\partial p^t_g}{\partial x^t_k} - \rho^t_{H^d_2} \frac{k^{w,t}_r}{\mu_w} k^{int}_{ij} \frac{\partial p^t_w}{\partial x^t_k} \tag{30}$$

$$L^{w,t}_j = (b-\phi) S^{g,t}_r \bar{\tau} D_{v/H_2} \rho_g \frac{\partial\left(\frac{\rho_v}{\rho_g}\right)}{\partial x^t_j} \qquad \text{and}$$
$$L^{g,t}_j = (b-\phi) S^{w,t}_r \bar{\tau} D_{H^d_2/w} \rho_w \frac{\partial\left(\frac{\rho_{H^d_2}}{\rho_w}\right)}{\partial x^t_j} \tag{31}$$

$$N^{w,t}_j = -\phi S^{g,t}_r \bar{\tau} D_{v/H_2} \rho_g \frac{\partial\left(\frac{\rho_v}{\rho_g}\right)}{\partial x^t_j} \qquad \text{and}$$
$$N^{g,t}_j = -\phi S^{w,t}_r \bar{\tau} D_{H^d_2/w} \rho_w \frac{\partial\left(\frac{\rho_{H^d_2}}{\rho_w}\right)}{\partial x^t_j} \tag{32}$$

$$C^{w,t} = \frac{\rho^B_w S^{w,B}_r}{\Delta t}\left(\phi^B + (b-\phi^A)\frac{V^B}{V^A}\right) + \frac{\rho^B_v S^{g,B}_r}{\Delta t}\left(\phi^B + (b-\phi^A)\frac{V^B}{V^A}\right)$$
$$C^{g,t} = \frac{\rho^B_{H^d_2} S^{g,B}_r}{\Delta t}\left(\phi^B + (b-\phi^A)\frac{V^B}{V^A}\right) + \frac{\rho^B_{H^d_2} S^{w,B}_r}{\Delta t}\left(\phi^B + (b-\phi^A)\frac{V^B}{V^A}\right) \tag{33}$$

$$F^{w,t}_i = f^t_{w,i} + f^t_{v,i} \qquad \text{and} \qquad F^{g,t}_i = f^t_{H_2,i} + f^t_{H^d_2,i} \tag{34}$$

$$M^{w,t} = \dot{M}_w + \dot{M}_v \qquad \text{and} \qquad M^{g,t} = \dot{M}_{H_2} + \dot{M}_{H^d_2} \tag{35}$$

Lastly, the two terms $\left[K^{w,t}\right]$ and $\left[K^{g,t}\right]$ are added in Eqs. (28) and (29) to consider the intrinsic permeability evolution. The constitutive Eqs. (50) and (51) of Section 4 are used to capture the effect of shear strain localisation on gas transport. For such a permeability evolution with the strain tensor, the two submatrices are then described as follows:

$$\left[K^{w,t}\right] = \left(\rho^t_w \frac{k^{w,t}_r}{\mu_w}\left(\frac{\partial p^t_w}{\partial x^t_j} + \rho^t_w g_j\right) + \rho^t_v \frac{k^{g,t}_r}{\mu_g}\left(\frac{\partial p^t_g}{\partial x^t_j} + \rho^t_g g_j\right)\right) \times \begin{bmatrix} \frac{\partial k^{int}_{1j}}{\partial \varepsilon_{11}} & \frac{\partial k^{int}_{1j}}{\partial \varepsilon_{12}} & \frac{\partial k^{int}_{1j}}{\partial \varepsilon_{21}} & \frac{\partial k^{int}_{1j}}{\partial \varepsilon_{22}} \\ \frac{\partial k^{int}_{2j}}{\partial \varepsilon_{11}} & \frac{\partial k^{int}_{2j}}{\partial \varepsilon_{12}} & \frac{\partial k^{int}_{2j}}{\partial \varepsilon_{21}} & \frac{\partial k^{int}_{2j}}{\partial \varepsilon_{22}} \\ 0 & 0 & 0 & 0 \end{bmatrix} \tag{36}$$

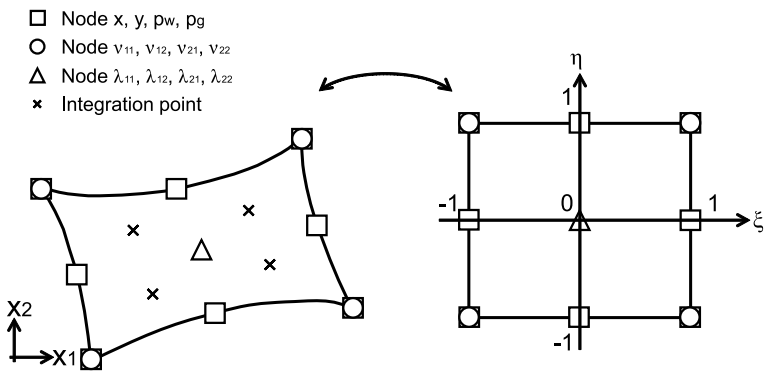

Fig. 2. 2D finite element SGRT used for the spatial discretisation of the model: current element and parent element.

$$\left[K^{g,t}\right] = \left(\rho^t_{H_2}\frac{k^{g,t}_r}{\mu_g}\left(\frac{\partial p^t_g}{\partial x^t_j}+\rho^t_g g_j\right)+\rho^t_{H_2^d}\frac{k^{w,t}_r}{\mu_w}\left(\frac{\partial p^t_w}{\partial x^t_j}+\rho^t_w g_j\right)\right) \times \begin{bmatrix} \frac{\partial k^{int}_{1j}}{\partial \epsilon_{11}} & \frac{\partial k^{int}_{1j}}{\partial \epsilon_{12}} & \frac{\partial k^{int}_{1j}}{\partial \epsilon_{21}} & \frac{\partial k^{int}_{1j}}{\partial \epsilon_{22}} \\ \frac{\partial k^{int}_{2j}}{\partial \epsilon_{11}} & \frac{\partial k^{int}_{2j}}{\partial \epsilon_{12}} & \frac{\partial k^{int}_{2j}}{\partial \epsilon_{21}} & \frac{\partial k^{int}_{2j}}{\partial \epsilon_{22}} \\ 0 & 0 & 0 & 0 \end{bmatrix} \tag{37}$$

From this formulation of the balance equations of the problem in matrix form, it is possible to spatially discretise the continuum medium in finite elements. In this work, the coupled finite element used to model the solid bodies is referred to as the SGRT element in the LAGAMINE code. This 2D isoparametric element is composed of eight nodes for the displacement fields u_i, the water pressure field p_w and the gas pressure field p_g, four nodes for the microkinematic gradient field ν_{ij} and one node for the Lagrange multiplier field λ_{ij} as presented in Fig. 2.

3. Numerical simulations

The numerical tool presented in this article is now applied to perform numerical simulations at nuclear waste disposal scale from the excavation time and over a period long enough (see Fig. 6(b)) to cope with gas generation and migration. The selected case study is close to the current design of a storage drift for long-lived intermediate-level waste (MAVL) according to the French concept managed by the ANDRA.[1] Practically, MAVL galleries are made up of several hundred metres in length, 10.4 m in excavated diameter, and of concrete structural support ensuring stability, and are drilled in a low-permeable rock called Callovo-Oxfordian claystone. In this section, the ingredients of the numerical simulations are presented, covering in particular the geometry of the problem, the mesh of the model, the initial boundary conditions as well as the successive steps of the simulations carried out by means of boundary conditions update.

3.1. Geometry

The configuration of the MAVL storage gallery consists in a circular section drift of radius $R = 5.2$ m, parallel to the major *in situ* principal stress. The initial conditions in the COx claystone for the considered orientation of the gallery (Fig. 3) are defined by an anisotropic stress state and a homogeneous water pressure as:

$$\sigma_{x,0} = 12.4 \text{ MPa}, \quad \sigma_{y,0} = 12.7 \text{ MPa}, \quad \sigma_{z,0} = \sigma_H = 16.1 \text{ MPa},$$
$$p_{w,0} = 4.7 \text{ MPa} \tag{38}$$

[1] Agence Nationale pour la gestion des Déchets RadioActifs.

where $\sigma_{x,0}$ is the minor horizontal principal total stress, $\sigma_{y,0}$ is the vertical principal total stress and $\sigma_{z,0}$ corresponds to the major horizontal principal total stress, while $p_{w,0}$ is the initial pore water pressure. As presented in Fig. 3, MAVL galleries are reinforced by structural concrete support ensuing stability, namely stuffing layers and precast arch segments. It is worth noting that these latter are modelled as a continuous shell, without considering the joints between the segments. This gives a final useable circular cross-section with a radius of 4.35 m.

In the treated problem, the HM modelling of the tunnel is performed in two-dimensional plane strain state. A schematic representation of the numerical model involving the mesh and the different boundary conditions is illustrated in Fig. 4. Assuming symmetries of the problem along the $x-$ and $y-$axes, only a quarter of the gallery cross-section is discretised. The geometry extension covers a domain of 300 m × 300 m in the horizontal and vertical directions, establishing two far field boundary conditions, and integrates a more refined discretisation close to the tunnel.

Concerning the boundary conditions, the initial stresses, pore water pressure and gas pressure are imposed constant at the mesh external boundaries. On the wall of the tunnel, the initial boundary conditions in terms of stresses and fluid pressures will be progressively adapted as a function of the successive phases of the simulation. Moreover, the symmetry condition is established along the symmetry axes by considering no normal displacements and impervious boundaries (water and gas flows blocked to zero). Regarding the second gradient boundary conditions, a special attention must be dedicated to the kinematic boundary conditions required to establish the symmetry, as stipulated in Zervos et al. (2001). The presence of gradient terms in the equilibrium equations (6) to (10) of the H^2M second gradient model requires that the radial displacement u_r must be symmetric on both sides of the symmetry axes. This supplementary kinematic condition implies that the normal derivative of u_r has to cancel with respect to the tangential direction θ, i.e. $\frac{\partial u_r}{\partial \theta} = 0$. Finally, natural boundary conditions for the double force $\dot{T}_i = 0$ are assumed on the different boundaries and gravity is not taken into account.

3.2. Boundary condition evolution

In practice, the three-step application discussed in this article is divided into the storage gallery excavation, the tunnel ventilation and finally the gas generation and migrations. This sequential evolution of the problem is translated into a boundary value problem which is carried out by progressively adjusting the boundary conditions using the finite-element code LAGAMINE. The drilling of the tunnel is performed with the convergence-confinement method which is an approximation method for tunnelling that allows transforming a whole three dimensional study of tunnel excavation into a two dimensional analysis in plane strain conditions, based on an identical gallery convergence assumption (Bernaud and Rousset, 1992). The effect of the excavation

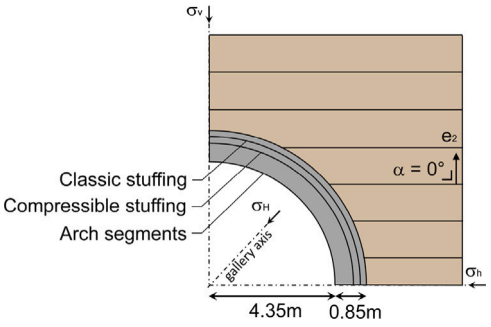

Fig. 3. Zoom on the refined support zone, with stress state definition and bedding planes orientation.

front progress is taken into account by applying a fictive pressure σ_r^Γ on the drift wall that depends on the vicinity of the excavation front to the studied drift section through a deconfinement rate ζ (Fig. 5(a)):

$$\sigma_r^\Gamma = (1-\zeta)\sigma_{r,0} \tag{39}$$

where σ_r^Γ is the total radial stress, $\sigma_{r,0}$ is the initial mechanical pressure on the gallery wall that corresponds to the initial stress in the material, and ζ is the deconfinement rate ranging from 0 to 1.

An excavation rate of 18 m per day is considered here, implying that the excavation front crosses the studied section after about 10 h and that the excavation is fully completed after about 24 h. The evolution of the deconfinement rate with time is detailed in Fig. 5(b) where the origin of the time axis corresponds to the moment when the studied section starts to be influenced by excavation of the previous sections of the tunnel. Pore water pressure at drift wall p_w^Γ is also affected during the excavation phase and starts to decrease quickly and linearly from its initial value towards the atmospheric pressure when the deconfinement starts. In addition, the stress imposition at the gallery wall is also conditioned by the support structure. Practically, the three layers of support are supposed to be applied simultaneously at 96% deconfining as depicted in Fig. 5(b).

So far, there is no ventilation inside the gallery which means that the air is fully saturated with water vapour. This maximum concentration corresponds to air with 100% of Relative Humidity (RH) according to Kelvin's law:

$$RH = \frac{p_v}{p_v^0} = \frac{\rho_v}{\rho_v^0} = exp\left(\frac{-p_c M_v}{\rho_w RT}\right) \tag{40}$$

where p_v is the partial pressure of water vapour, p_v^0 is the pressure of saturated water vapour, and ρ_v^0 is the saturated vapour concentration, M_v is the molar mass of water vapour, $R = 8.314$ [J/mol K] is the gas constant and $T = 298.15$ [K] is the absolute temperature.

Afterwards, the drift is ventilated during the operation phase in order to regulate the temperature according to workers needs. The ventilation imposes a RH of about 70% which modifies the hydraulic boundary condition at the drift wall by reducing the pore water pressure from 0.1 MPa to −49.1 MPa. This process is initiated 35 days after the excavation starts, the RH is progressively decreased during a period of 3 months to reach the planned value of P_w after 125 days as exposed in Fig. 6(a). Ventilation is then maintained constant in the tunnel during an exploitation period of about 100 years. Modelling this ventilation phase is of particular interest since the generated suction may drain the water from the rock through the support, desaturate it, and thence modify the fracturing pattern as well as the size of the fractured zone.

Finally, after the 100-year phase of ventilation, the storage gallery is supposed to be entirely filled with waste packages, properly sealed and closed. From this time, the system becomes impervious to water and a period of pore water pressures stabilisation initiates since there is no more drainage imposed by the ventilation of the drift. It is worth noting that concurrently to the installation of the canisters, a significant rise in temperature takes place around the storage but this effect falls beyond the scope of the present study. Subsequently, gas starts to be generated in the form of hydrogen arising from steel corrosion. Hydrogen migrations are simulated by imposing a variation of gas pressures at the intrados of the support structure according to the H_2-profile given in Fig. 6(b) (Talandier, 2005). This last phase ranges from 100 years to a million years, with peak value of gas pressures reached around 66 000 years.

4. Constitutive models and parameters

The constitutive models of the Callovo-Oxfordian claystone and the support and their related parameters required for the numerical application are presented in this section. The hydro-mechanical description of the COx behaviour includes a mechanical model for the classical first gradient part related to the macrostructure, a mechanical model for the second gradient part related to the microstructure and a hydraulic model to reproduce water and gas flows in the partially saturated porous medium.

4.1. Callovo-oxfordian claystone behaviour

4.1.1. First gradient mechanical model

An elasto-viscoplastic model with cross-anisotropy and horizontal isotropic bedding planes is considered for the rock, which can be decomposed into elastic, plastic and viscous components.

Elastic component

The linear elastic behaviour of the rock is based on the classical Hooke's law linking the stress rate $\dot{\sigma}_{ij}^e$ to the reversible strain rate component $\dot{\varepsilon}_{kl}^e$:

$$\dot{\sigma}_{ij}^e = C_{ijkl}^e\ \dot{\varepsilon}_{kl}^e \iff \dot{\varepsilon}_{ij}^e = D_{ijkl}^e\ \dot{\sigma}_{kl}^e \tag{41}$$

where C_{ijkl}^e is the elastic stiffness tensor and D_{ijkl}^e is the elastic compliance tensor that is the inverse of the matrix C_{ijkl}^e. For cross-anisotropic materials (Lekhnitskii, 1963) such as the COx formation, the behaviour remains isotropic in the parallel bedding planes which requires 5 independent parameters to express the elastic compliance tensor (Amadei, 1983):

$$\begin{cases} E_1 = E_3 = E_\parallel, & E_2 = E_\perp \\ \nu_{13} = \nu_{31} = \nu_{\parallel\parallel}, & \nu_{12} = \nu_{32} = \nu_{\parallel\perp}, \quad \nu_{21} = \nu_{23} = \nu_{\perp\parallel} \\ G_{12} = G_{32} = G_{\parallel\perp}, & G_{13} = \dfrac{E_\parallel}{2(1+\nu_{\parallel\parallel})} = G_{\parallel\parallel} \end{cases} \tag{42}$$

where the subscripts ∥ and ⊥ refer respectively to the direction parallel to the isotropic bedding plane (directions 1 and 3 here) and perpendicular to the bedding (direction 2).

Plastic component

The elastoplastic behaviour of the COx claystone is characterised by an internal friction model with a non-associated plasticity and a Van Eekelen yield surface f (Van Eekelen, 1980) (under soil mechanics convention with positive compressive stress) defined as:

$$f \equiv I I_{\hat{\sigma}} - m\left(I_\sigma + \frac{3c}{\tan\phi}\right) = 0 \tag{43}$$

where c is the cohesion, ϕ is the friction angle, m is a parameter of the yield surface which introduces the dependence to the Lode angle, $I_{\sigma'} = \sigma'_{ij}\delta_{ij} = \sigma'_{ii}$ is the first invariant of stresses, $II_{\hat{\sigma}'} = \sqrt{0.5\hat{\sigma}'_{ij}\hat{\sigma}'_{ij}}$ is the second invariant of deviatoric stresses, $\hat{\sigma}'_{ij}$ is the deviatoric part of the effective stress tensor.

Furthermore, the model allows isotropic hardening or softening for the cohesion and the friction angle upon loading. A plot of the yield surface in the plane of the first and second invariants of stresses is presented in Fig. 7(a). Further details about the model are available in Pardoen et al. (2015b). The elastoplastic parameters of the COx claystone, reported in

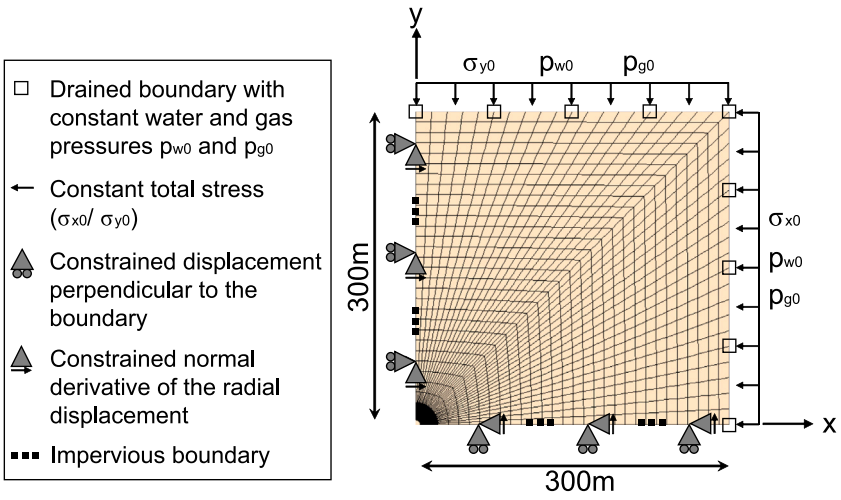

Fig. 4. Geometry and boundary conditions of the 2D plane strain model.

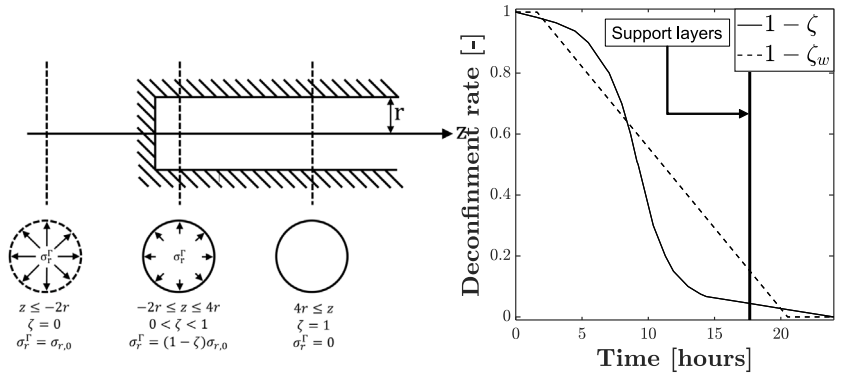

Fig. 5. (a) Theory of deconfinement rate during drift excavation, (b) applied deconfinement curves for the total radial stress and for the pore water pressure during drift excavation.

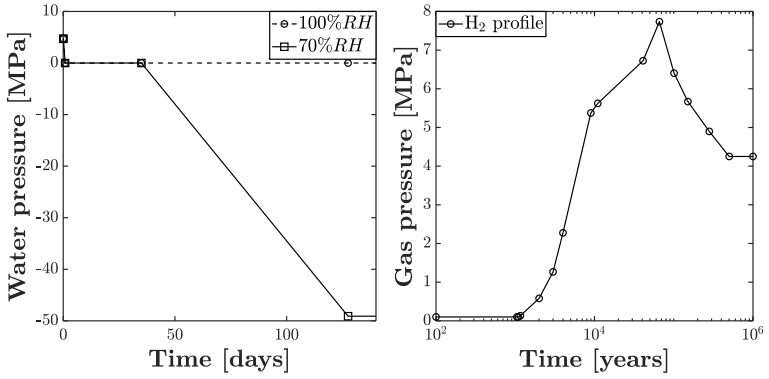

Fig. 6. (a) profile of pore water pressures with ventilation and (b) profile of gas pressures.

Table 1 are taken from Argilaga et al. (2019), after (Pardoen and Collin, 2017) where calibration is realised based on experimental data.

Viscoplastic component

Viscoplasticity is also taken into account to reproduce the creep deformations characterising the long term behaviour of the claystone (Shao et al., 2003). The approach adopted hereafter consists in a single viscoplastic flow mechanism decoupled from elastoplasticity, with the following viscoplastic loading surface f^{vp} (Fig. 7(b)) controlled by a delayed viscoplastic hardening function α^{vp} (Jia et al., 2008; Zhou et al., 2008):

$$f^{vp} \equiv \sqrt{3} I I_{\hat{\sigma}} - \alpha^{vp} R_c \sqrt{A\left(C_s + \frac{I'_\sigma}{3R_c}\right)} = 0 \tag{44}$$

$$\alpha^{vp} = \alpha_0^{vp} + \left(1 - \alpha_0^{vp}\right) \frac{\varepsilon_{eq}^{vp}}{B^{vp} + \varepsilon_{eq}^{vp}} \tag{45}$$

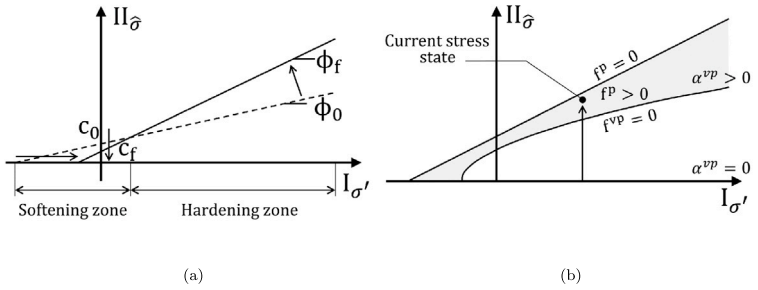

Fig. 7. (a) Van Eekelen yield surface and (b) viscoplastic surface in effective stress invariant plane.

where R_c is the uniaxial compressive strength, A is an internal friction coefficient, C_s is a constant cohesion coefficient, α_0^{vp} is the initial threshold for the viscoplastic flow, B^{vp} is a hardening parameter, and ε_{eq}^{vp} is the equivalent viscoplastic strain. A complete description of the viscoplastic model is available in Jia et al. (2008) and Zhou et al. (2008) and details about its implementation in the gallery excavation can be found in Pardoen and Collin (2017). The viscoplastic parameters of the COx claystone, detailed in Table 2, are taken from Argilaga et al. (2019), after (Pardoen and Collin, 2017) and calibrated against laboratory tests.

4.1.2. Second gradient mechanical model

The second gradient mechanical model gives an additional constitutive stress–strain relation between the kinematics and the stress at microscale. Based on Mindlin (1965), it is an isotropic linear elastic law depending on one constitutive elastic parameter D in its simplified version proposed in Matsushima et al. (2002). This elastic modulus symbolises the physical microstructure and is related to the internal length scale relevant for the shear band width (Chambon et al., 1998; Collin et al., 2009).

4.1.3. Hydraulic model

In the hydraulic model used for the COx claystone, the transfer of the liquid phase (water and gas) by advection in an unsaturated porous medium is defined by the generalised Darcy's law (Darcy, 1856):

$$q_{w,i} = -\frac{k_{ij}^{int} k_r^w}{\mu_w}\left(\frac{\partial p_w}{\partial x_j} + \rho_w g_j\right) \quad \text{and} \quad q_{g,i} = -\frac{k_{ij}^{int} k_r^g}{\mu_g}\left(\frac{\partial p_g}{\partial x_j} + \rho_g g_j\right) \tag{46}$$

where k_r^w and k_r^g are the water and gas relative permeabilities, μ_w and μ_g are the dynamic viscosities of water and gas respectively, and k_{ij}^{int} is the anisotropic tensor of intrinsic permeability of the material, defined by two components $k_{\parallel}$ and $k_{\perp}$ respectively parallel and perpendicular to the isotropic planes:

$$k_{ij} = \begin{bmatrix} k_{\parallel} & 0 & 0 \\ 0 & k_{\perp} & 0 \\ 0 & 0 & k_{\parallel} \end{bmatrix} \tag{47}$$

The material retention behaviour is represented by a retention curve (Fig. 8(a)) of van Genuchten's type (Van Genuchten, 1980), linking the capillary pressure to the degree of water saturation:

$$S_r^w = S_{res} + (S_{max} - S_{res})\left(1 + \left(\frac{s}{P_r}\right)^{\frac{1}{1-\mathcal{F}}}\right)^{-\mathcal{F}} \tag{48}$$

where P_r is the air entry pressure, S_{max} and S_{res} are the maximum and residual degrees of water saturation, $\mathcal{F}$ is a model parameter, and s is the suction.

On the other hand, permeabilities evolve with the degree of saturation, defining relative permeability curves. The Mualem–van Genuchten's model (Mualem, 1976) is used to express the water relative permeability (Fig. 8(b)) while a cubic law (Charlier et al., 2013) is generally adopted to describe the gas relative permeability (Fig. 8(c)):

$$k_r^w = \sqrt{S_r^w}\left(1 - \left(1 - S_r^{w\frac{1}{\mathcal{M}}}\right)^{\mathcal{M}}\right)^2 \quad \text{and} \quad k_r^g = (1 - S_r^w)^3 \tag{49}$$

where S_r^w is the degree of water saturation, and $\mathcal{M}$ is a model parameter.

On top of that, enhanced HM couplings are introduced in the model. In order to capture the effects of shear strain localisation in band mode, a strain-dependent isotropic evolution of the hydraulic permeability tensor is taken into account based on a power (cubic) formulation (Pardoen et al., 2014):

$$k_{ij} = k_{ij,0}\left(1 + \beta_{per}\langle YI - YI^{thr}\rangle \hat{\varepsilon}_{eq}^3\right) \tag{50}$$

where $k_{ij,0}$ is the initial intrinsic permeability tensor, β_{per} is an evolution parameter, $\hat{\varepsilon}_{eq}^p$ is taken as the Von Mises' equivalent deviatoric plastic strain, YI is the yield index and YI^{thr} is a threshold value below which there is no intrinsic permeability variation.

The second enhanced HM coupling deals with the evolution of the water retention curve with strain (Gerard et al., 2012) and is included in the model to consider the effect of the modification of the pore network morphology on the water retention property of the material. Practically, the evolution of the parameter P_r, standing for the gas (Hydrogen) entry value in Van Genuchten's model is correlated to the permeability evolution (see Gerard (2011) for further details):

$$P_r = P_{r,0}\frac{\sqrt[3]{k_{ij,0}}}{\sqrt[3]{k_{ij}}} \tag{51}$$

where P_r is the current gas entry pressure, $P_{r,0}$ is the initial value of gas entry pressure, k_{ij} is the current permeability and $k_{ij,0}$ is the initial permeability. This expression of the air entry pressure is then introduced in the retention curve formulation. The hydraulic parameters of the COx claystone, reported in Table 3, are taken from Pardoen and Collin (2017), after (Charlier et al., 2013) where a synthesis of the claystone parameters is detailed. The calibration is obtained from laboratory experiments and results available in the literature.

4.1.4. Effective stress definition

In the context of unsaturated and anisotropic material dealing with water and gas, Bishop's formulation of effective stresses presented in Eq. (8) is used. In this expression, the Biot's tensor is expressed in orthotropic axes according to Eq. (20). The prescribed values of parallel and perpendicular Biot's coefficients for the COx claystone are respectively given by $b_{\parallel} = 0.6$ and $b_{\perp} = 0.64$.

4.2. Support behaviour

As exposed in Section 3, MAVL drifts are reinforced by different layers of support with the aim of avoiding partial collapse of the tunnel during drilling operations and limiting convergence of the surrounding rock. Practically, the classic and compressible stuffing layers have a

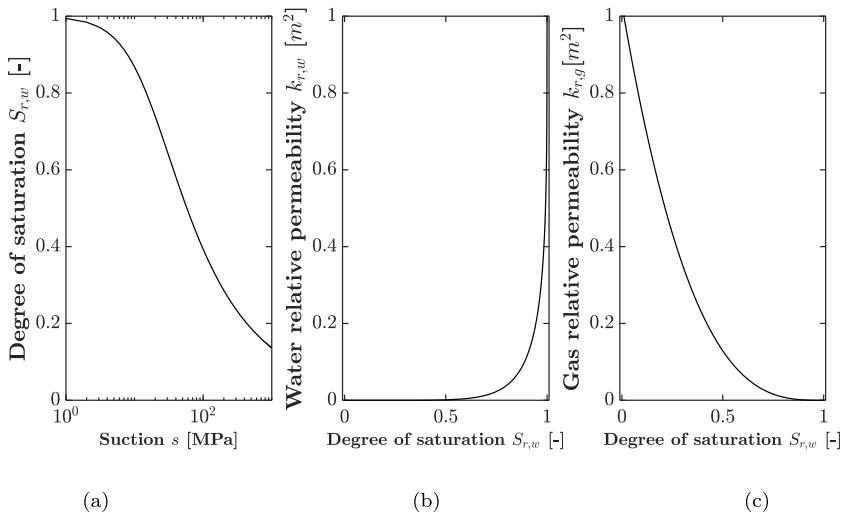

Fig. 8. Definition of (a) water retention curve, (b) water relative permeability and (c) gas relative permeability.

Table 1
Set of COx elastoplastic mechanical parameters.

	Parameter	Symbol	Value	Unit
Geomechanical	Parallel Young's modulus	$E_{\parallel}$	5	[GPa]
	Perpendicular Young's modulus	$E_{\perp}$	4	[GPa]
	Poisson's ratio	$\nu_{\parallel\parallel}$	0.24	[−]
	Poisson's ratio	$\nu_{\parallel\perp}$	0.325	[−]
	Poisson's ratio	$\nu_{\perp\parallel}$	0.26	[−]
	Shear modulus	$G_{\parallel\perp} = G_{\perp\parallel}$	1.63	[GPa]
	Shear modulus	$G_{\parallel\parallel}$	2.016	[GPa]
	Parallel Biot's coefficient	$b_{\parallel}$	0.6	[−]
	Perpendicular Biot's coefficient	$b_{\perp}$	0.64	[−]
	Solid grain density	ρ_s	2750	[kg/m^3]
	Initial cohesion	c_i	4.1 (0°)	[MPa]
	Cohesion parameter	A_{11}	0.117	[−]
	Cohesion parameter	b_1	14.236	[−]
	Ratio of cohesion softening	ξ_c	5	[−]
	Cohesion softening parameter	B_c	0.003	[−]
	Initial compressive friction angle	$\varphi_{c,0}$	10	[°]
	Final compressive friction angle	$\varphi_{c,f}$	23	[°]
	Initial extensive friction angle	$\varphi_{e,0}$	7	[°]
	Final extensive friction angle	$\varphi_{e,f}$	23	[°]
	Friction angle hardening parameter	B_{φ}	0.001	[−]
	Dilatancy angles	$\psi_c = \psi_e$	0.5	[°]
Microstructure	Second gradient elastic modulus	D	14.016	[kN]

thickness of 0.15 m and 0.2 m respectively while the arch segments are 0.5 m thick. The concrete arch segments and the classic stuffing layer are characterised by an elastoplastic mechanical behaviour while the compressible stuffing layer is assumed to have a linear elastic behaviour. The mechanical parameters of the support layers are retrieved from Andra (2016) and Gerard et al. (2008) and gathered in the first part of Table 4. Hydraulically, the same model as for the COx claystone (described in Eqs. (46) to (49)) is used for the support, without considering any evolution of hydraulic properties with strain. The specific hydraulic parameters assigned to each layer of the support are gathered in the second part of Table 4.

5. Results and discussion

To emphasise the effect of the EDZ on gas migrations, three modelling cases are investigated. In the first reference simulation, the development of the EDZ is supposed to induce no alteration of the hydraulic properties in this zone. In the two subsequent simulations, the enhanced couplings between fluids transfers (water and gas) and the mechanical behaviour of the fractured zone are taken into account. First, a strain-dependent evolution of the material intrinsic permeability is envisaged, subsequently enriched by the modification of the water retention property with the deformation.

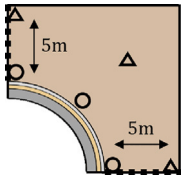

Fig. 9. Definition of cross-section and observation points for the results.

Various numerical results computed with the finite element code LAGAMINE are presented and analysed hereafter for the studied section and in terms of temporal evolutions in selected points of this section (Fig. 9).

Table 2
Set of COx viscoplastic mechanical parameters.

	Parameter	Symbol	Value	Unit
Viscoplastic	Uniaxial compressive strength	R_c	21	[MPa]
	Internal friction coefficient	A^{vp}	2.62	[−]
	Cohesion coefficient	C^{vp}	0.03	[−]
	Viscoplastic potential parameter	β^{vp}	1.1	[−]
	Initial threshold for the VP flow	α_0^{vp}	0.142	[−]
	Reference fluidity	γ_0	700	[s^{-1}]
	Temperature parameter	γ_1	57×10^3	[J/mol]
	Creep curve shape parameter	$\mathcal{N}$	5.0	[−]
	VP hardening function parameter	B^{vp}	7.5×10^{-2}	[−]

Table 3
Set of COx hydraulic parameters.

	Parameter	Symbol	Value	Unit
Hydraulic	Initial porosity	n	0.173	[−]
	Initial parallel intrinsic permeability	$k_{w,\parallel,0}$	4×10^{-20}	[m^2]
	Initial perp. intrinsic permeability	$k_{w,\perp,0}$	1.33×10^{-20}	[m^2]
	Water density	ρ_w	1000	[kg/m^3]
	H_2 density	ρ_{H_2}	0.0794	[kg/m^3]
	Water dynamic viscosity	μ_w	0.001	[Pa s]
	H_2 dynamic viscosity	μ_{H_2}	9×10^{-6}	[Pa s]
	Water compressibility	χ_w^{-1}	5×10^{-10}	[Pa^{-1}]
	H_2 Henry coefficient	H_i	0.0193	[−]
	Air entry pressure (1^{st} coeff. of S_r^w)	P_r	15	[MPa]
	Parameter (2^{nd} coeff. of S_r^w)	$\mathcal{F}$	1.49	[−]
	Parameter (1^{st} coeff. of k_r^w)	$\mathcal{M}$	0.32886	[−]
	Max. degree of water saturation	S_{max}	1	[−]
	Residual degree of water saturation	S_{res}	0.01	[−]
	Evolution parameter	β_{perm}	10^{10}	[−]
	Permeability variation threshold	ε_{eq}^{thr}	0.01	[−]
	Tortuosity	τ	0.25	[−]

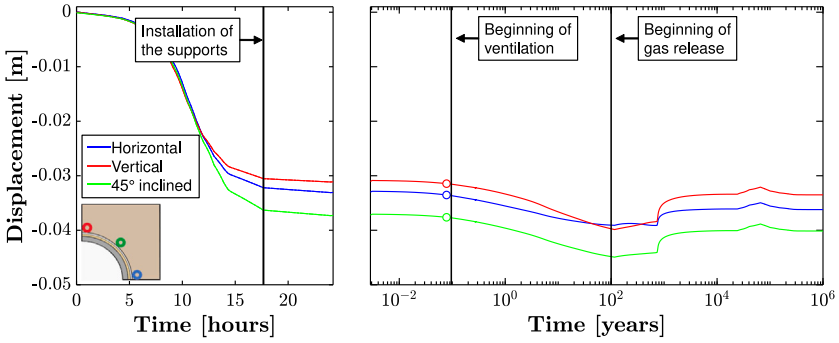

(a) Excavation phase (b) Ventilation and gas migration phases

Fig. 10. Long-term convergence induced by the successive phases of the simulation.

5.1. Reference simulation

The first performed simulation focuses on the development of the EDZ following the drilling process. The main purpose is to characterise the extent of fractures induced by rock deconfinement during the excavation phase. These fractures are reproduced by shear banding and no modification of the hydraulic properties in the damaged zone is taken into account in this first simulation. Analysing first the results in terms of convergence in Fig. 10 offers a good overview of the drift behaviour throughout the simulations. For the considered drift, most part of the short-term radial displacement is due to the excavation process and the remainder of the displacement comes from the initiation of the ventilation phase. Viscosity is responsible of the long-term convergence of the system in Fig. 10(b). Once the stress imposed by ventilation is released and gas starts to be injected, the system progressively reconfines, leaving a residual radial displacement. This displacement is not uniform over the circumference because of inherent anisotropies and stress redistribution. Time captures of the increments of vertical and horizontal displacements at the end of the excavation are given in Fig. 11, which confirms a slightly more important convergence vertically.

The creation and evolution of the fractured zone can then be observed through the evolution of the shear strain localisation. The numerical results are presented in terms of Von Mises' equivalent deviatoric total strain (total deviatoric strain), the plastic zone, i.e. the plastic loading integration points (red squares), and the deviatoric strain increment, which represents the shear band activity:

$$\kappa_{eq} = \frac{\dot{\hat{\varepsilon}}_{eq} dt}{\int \dot{\hat{\varepsilon}}_{eq} dt} \tag{52}$$

where κ_{eq} is the deviatoric strain increment, $\hat{\varepsilon}_{eq} = \sqrt{\frac{2}{3}\hat{\varepsilon}_{ij}\hat{\varepsilon}_{ij}}$ is the total deviatoric strain, and $\hat{\varepsilon}_{ij} = \varepsilon_{ij} - \frac{\varepsilon_{kk}}{3}\delta_{ij}$ is the deviatoric part of the strain tensor.

Table 4
Set of parameters used in the different constitutive laws of the sustaining structure: classic stuffing, compressible stuffing and arch segments.

	Parameter	Symbol	Value	Unit
Classic stuffing	Elastic Young's modulus	E	17.5	[GPa]
	Poisson'ratio	ν	0.25	[−]
	Friction angle	φ	30	[°]
	Cohesion	c	2.94	[MPa]
	Density	ρ	2300	$[\frac{kg}{m^3}]$
Compressible stuffing	Elastic Young's modulus	E	0.1	[GPa]
	Poisson's ratio	ν	0.0	[−]
	Density	ρ	2300	$[\frac{kg}{m^3}]$
Arch segments	Elastic Young's modulus	E	39	[GPa]
	Poisson's ratio	ν	0.2	[−]
	Friction angle	φ	38	[°]
	Cohesion	c	14.6	[MPa]
	Density	ρ	2650	$[\frac{kg}{m^3}]$
Compressible stuffing	Initial porosity	n	0.25	[−]
	Initial parallel intrinsic permeability	$k_{w,\parallel,0}$	10^{-15}	[m^2]
	Initial perp. intrinsic permeability	$k_{w,\perp,0}$	10^{-15}	[m^2]
	Air entry pressure (1st coeff. of S_r^w)	P_r	1	[MPa]
	Parameter (2nd coeff. of S_r^w)	$\mathcal{G}$	1.54	[−]
	Parameter (1st coeff. of $k_{r,w}$)	$\mathcal{F}$	0.3507	[−]
	Max. degree of water saturation	S_{max}	1	[−]
	Residual degree of water saturation	S_{res}	0.01	[−]
	Tortuosity	τ	0.25	[−]
Compressible stuffing	Initial porosity	n	0.5	[−]
	Initial parallel intrinsic permeability	$k_{w,\parallel,0}$	10^{-10}	[m^2]
	Initial perp. intrinsic permeability	$k_{w,\perp,0}$	10^{-10}	[m^2]
	Air entry pressure (1st coeff. of S_r^w)	P_r	0.2	[MPa]
	Parameter (2nd coeff. of S_r^w)	$\mathcal{G}$	1.54	[−]
	Parameter (1st coeff. of $k_{r,w}$)	$\mathcal{F}$	0.3507	[−]
	Max. degree of water saturation	S_{max}	1	[−]
	Residual degree of water saturation	S_{res}	0.01	[−]
	Tortuosity	τ	0.25	[−]
Arch segments	Initial porosity	n	0.15	[−]
	Initial parallel intrinsic permeability	$k_{w,\parallel,0}$	10^{-18}	[m^2]
	Initial perp. intrinsic permeability	$k_{w,\perp,0}$	10^{-18}	[m^2]
	Air entry pressure (1st coeff. of S_r^w)	P_r	5	[MPa]
	Parameter (2nd coeff. of S_r^w)	$\mathcal{G}$	1.54	[−]
	Parameter (1st coeff. of $k_{r,w}$)	$\mathcal{F}$	0.3507	[−]
	Max. degree of water saturation	S_{max}	1	[−]
	Residual degree of water saturation	S_{res}	0.01	[−]
	Tortuosity	τ	0.25	[−]

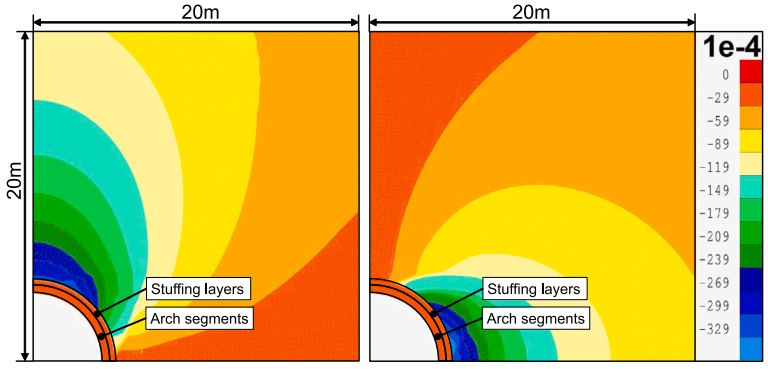

(a) Δy (b) Δx

Fig. 11. Variation of (a) vertical and (b) horizontal displacements at the end of the excavation.

From previous analyses (Pardoen et al., 2015a), it has been demonstrated that results from a quarter of a drift can be extrapolated to the full section drift provided that the specific second gradient boundary condition is well used (Zervos et al., 2001). Hence, Fig. 12 illustrates the creation of the fractured zone through the evolution of strain localisation around a full storage drift in the course of the excavation process. During the first part of the drilling, the deformation develops homogeneously around the drift. Then, the growth of a clear and well-constructed shear band pattern starts by the end of the deconfinement. The complete formation of the shear bands happens at about 96% deconfining, just before the installation of the support layers. The strain localisation initiates in the zone under plastic loading that appears in the vicinity of the storage drift. The onset and shape of this strain localisation zone can be attributed to the anisotropy of the material as

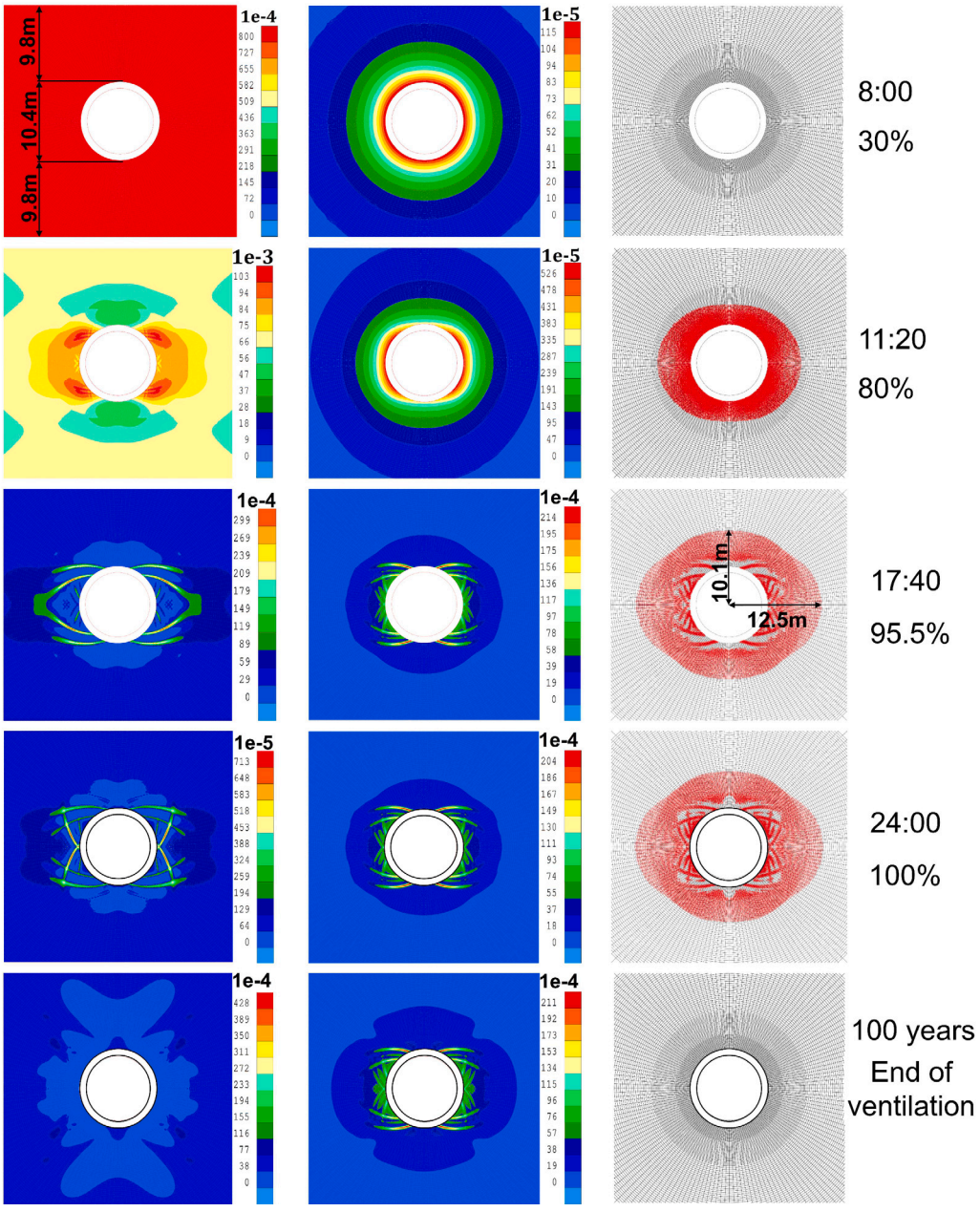

Fig. 12. Development of shear bands during the excavation process: (a) deviatoric strain increment, (b) total deviatoric strain and (c) plastic loading points.

well as of the initial stress state (Pardoen et al., 2015a). Since this initial stress state is not perfectly isotropic, the plastic zone appears to extent preferentially in the direction of the minor principal stress, namely horizontally. Within this fractured zone, shear bands initiate primarily from lateral edges of the tunnel. This preferential development of shear bands can be related to the evolution of cohesion around the drift (Pardoen and Collin, 2017), as presented in Fig. 13. Due to the loading evolution engendered by the drilling, cohesion softening occurs at the drift wall. This decrease in cohesion is more pronounced in the horizontal direction than in the vertical one. It tends to trigger the appearance of shear bands in this direction since the strength of the material is the lowest in this zone. By the end of the excavation process, the plastic zone has expanded over 7 m in the horizontal direction and 5 m in the vertical direction. Compared to the case of an unsupported drilling process, the installation of the support has the consequences of limiting the points in plastic charge and inhibiting any further development of localisation.

In the following, various numerical results are presented to emphasise the influence of the drift air ventilation. First, the time evolution of pore water pressure close to the drift wall is exhibited in Fig. 14. These curves details the progressive update in water pressures from the initial condition of $p_w = 4.7$ MPa to the atmospheric pressure imposed by the deconfinement during the excavation and then up to $p_w = -35$ MPa during the ventilation. As expected, the effect of the suction imposed at the intrados of the drift is highlighted by the progressive drainage of the rock mass, which tends to propagate further in the horizontal direction due to the anisotropy of permeability ($k_{w,\parallel,0} > k_{w,\perp,0}$ in Table 3). This

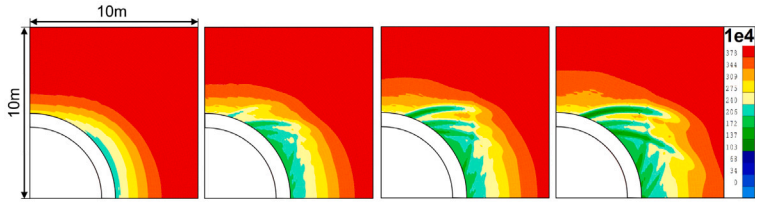

(a) 80% (b) 90% (c) 92.5% (d) 95.5%

Fig. 13. Evolution of cohesion during the excavation process.

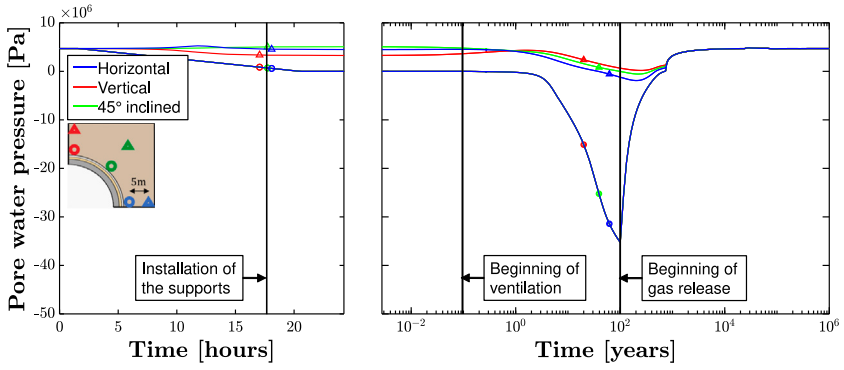

(a) Excavation phase (b) Ventilation and gas migration phases

Fig. 14. Time evolution of pore water pressure during the successive phases of the simulation, for the reference simulation.

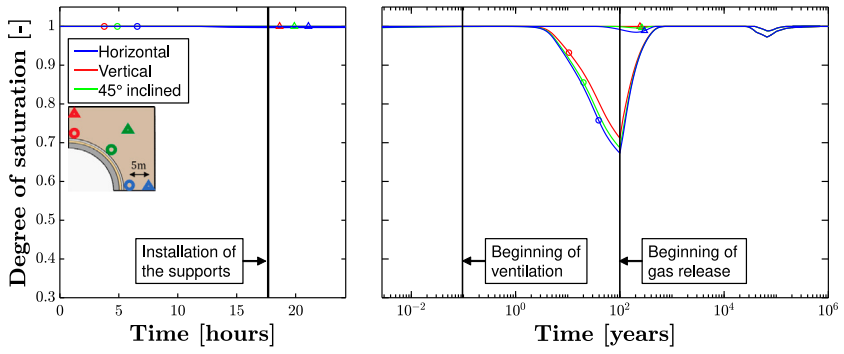

(a) Excavation phase (b) Ventilation and gas migration phases

Fig. 15. Time evolution of the degree of saturation during the successive phases of the simulation, for the reference case.

drainage is delayed by the concrete layer that acts as a buffer because of its low transfer properties.

In parallel, the time evolution of the water degree of saturation in the vicinity of the drift wall is illustrated in Fig. 15. During the excavation, the claystone remains almost fully saturated, while a significant reduction of the saturation appears throughout the phase of ventilation, resulting in a partially saturated zone over a distance of approximately 5 m in the rock. This strong desaturation observed close to the support is also consistent with the values of S_r given by the water retention curve 8(a) for the evolution of suction displayed in Fig. 14(b).

Moreover, the drainage of the rock together with the related desaturation around the drift causes the plastic zone to progressively become elastic again as highlighted in Fig. 12 (between 1 day and the end of ventilation). Integration points that were under plastic loading are now subjected to elastic unloading. It actually stems from the hydro-mechanical coupling inherent to Bishop's effective stress definition of Eq. (8). Considering this expression under constant total stress, any decrease in pore water pressure intrinsically implies an increase in the effective stress, which consequently engenders an enhancement of the material strength, i.e. a consolidation.

The evolution of effective stresses can be visualised by plotting the stress paths in the drift wall zone, as shown in Fig. 16 where $I_{\sigma'} = \sigma'_{ij}\delta_{ij} = \sigma'_{ii}$ is the first invariant of stresses, $II_{\hat{\sigma}'} = \sqrt{0.5\hat{\sigma}'_{ij}\hat{\sigma}'_{ij}}$ is the second invariant of deviatoric stresses, $\hat{\sigma}'_{ij}$ is the deviatoric part of the effective stress tensor.

In the course of the excavation phase, the radial stress tends to decrease and vanish at the gallery wall while the orthoradial stress is increased. This results in an overall increase in the deviatoric stress invariant until the stress state reaches the plastic criterion. In case of ventilation, an increase in effective stresses and consequently in the first stress invariant is noted around the drift owing to the imposed negative pore water pressure. This coupled response is well reflected in the

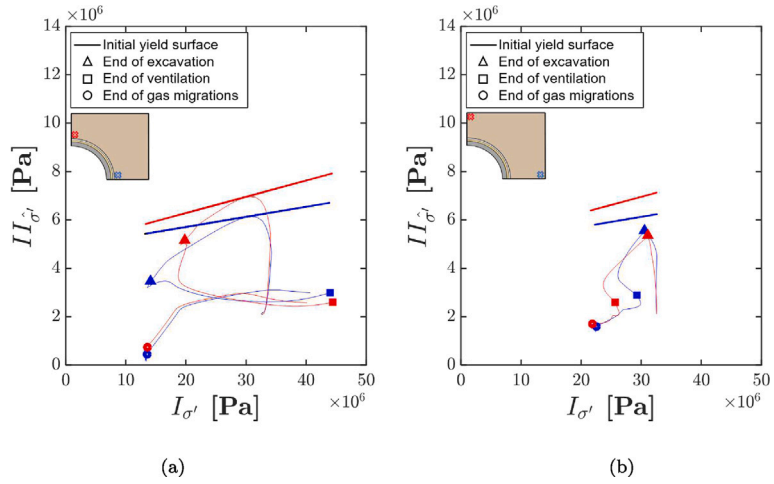

Fig. 16. Evolution of the stress paths during the simulation: (a) at the drift wall, (b) at a distance of 5 m from the drift wall.

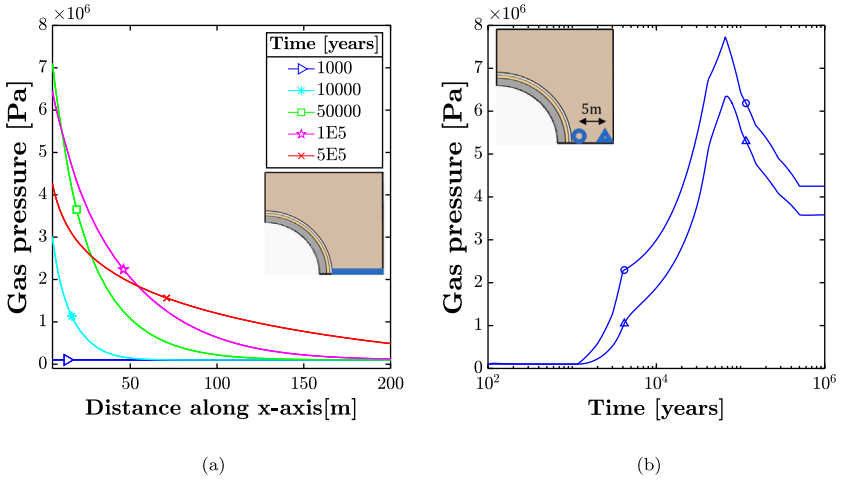

Fig. 17. Evolution of gas (Hydrogen) pressures (a) over the domain and (b) with time.

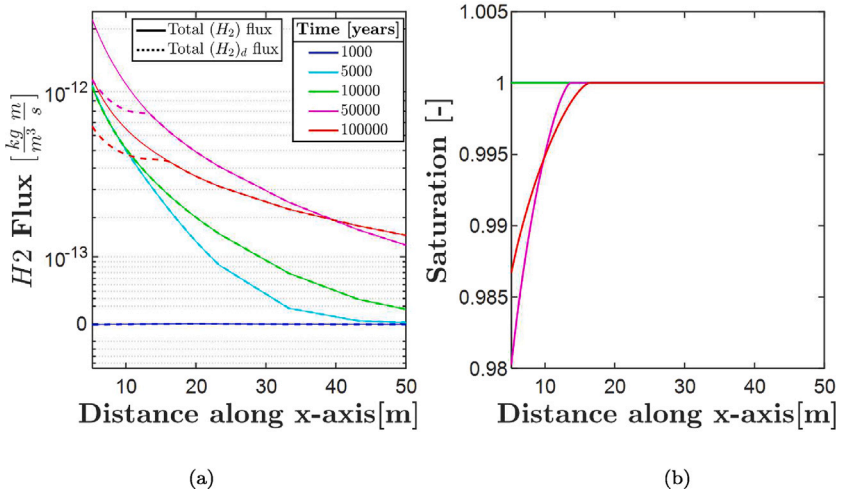

Fig. 18. (a) Comparison between dissolved Hydrogen and total Hydrogen flux (log scale along Y-axis (Webber, 2013)) and (b) corresponding saturation profiles.

corresponding stress path at the drift wall but is less discernible further away in the rock mass.

Finally, gas transfers in the form of Hydrogen take place in the long-term part of the simulation, according to the evolution profile given in Section 3. In Fig. 17(a), gas pressure profiles are displayed along the horizontal section of the domain, highlighting the progressive propagation of Hydrogen across the rock mass. The temporal evolution of gas pressures in the zone adjacent to the drift wall is presented

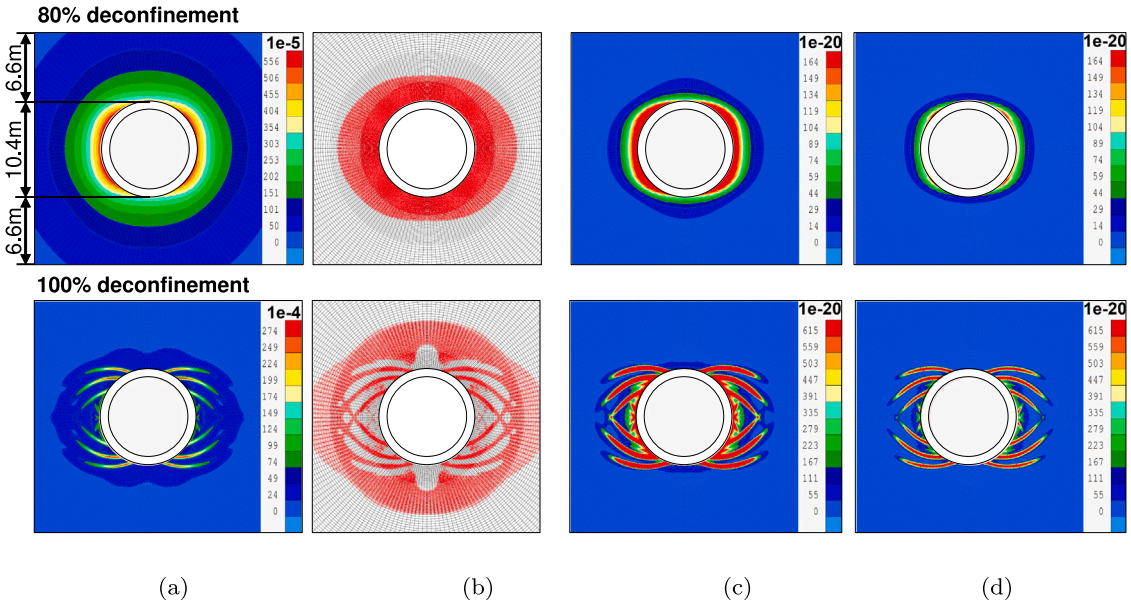

Fig. 19. Development of shear bands and evolution of water permeability at the end of excavation: (a) total deviatoric strain, (b) plastic loading points, and intrinsic water permeability in the (c) horizontal and (d) vertical directions.

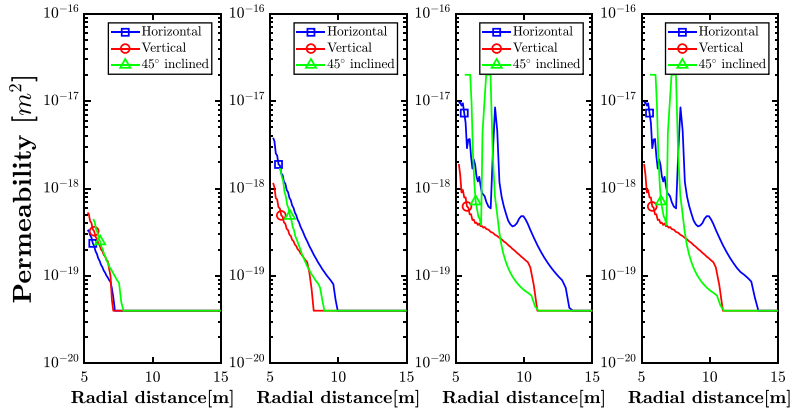

Fig. 20. Variation of parallel intrinsic permeability $k_{w,\parallel}$ as a function of the radial distance for different time steps.

in Fig. 17(b). By referring to the time evolution of water pressure (Fig. 14(b)), it comes out that the release of Hydrogen materialised by an increase in gas pressure starts after a period of approximately 1000 years when the pore water pressure has almost recovered the initial value of 4.7 MPa. No water overpressure is observed subsequently as a result of this rise in gas pressure.

A maximum gas pressure of about 7.5 MPa is reached at the drift wall after a period of around 60 000 years. Referring to the temporal evolution of the water degree of saturation in Fig. 15(b) points out that a desaturation of a few percent is associated to this peak of Hydrogen pressure. Desaturation profiles in the rock mass are illustrated in Fig. 18(b) and put into perspective with the dissolved and total Hydrogen flows profiles displayed in Fig. 18(a) in log scale (Webber, 2013). Close to the injection zone, it appears that dissolved gas in the water phase is not sufficient enough to ensure transfers of Hydrogen in the claystone rock under the largest Hydrogen production sequences. This quantity of dissolved Hydrogen is indeed physically limited by Henry's law, which leads to the creation of a gaseous phase, and to the desaturation of argillite over a certain radial distance. Since total Hydrogen fluxes decrease with the radial distance, dissolved hydrogen becomes predominant again at the transition between saturated and partially saturated zones.

5.2. Evolution of the water intrinsic permeability with the deformations

So far, the behaviour of the EDZ has been limited to the development of fractures in the form of shear strain localisation bands. However, this process of fracture generation tends also to substantially affect the flow properties of the in-situ material. In this second part of the simulations, an advanced coupled hydro-mechanical behaviour of the EDZ is considered in order to end up with a more accurate representation of the phenomena related to gas migration. As detailed in Section 3, the impact of fracturing on the flow transfer characteristics is addressed by relating the intrinsic permeability evolution with the mechanical deformations according to expression (50).

The variations in (parallel and perpendicular) intrinsic water permeabilities around the drift are presented at the end of the excavation process in Figs. 19(c) and 19(d) respectively, and put into perspective with the creation of the plastic zone in Figs. 19(a) and 19(b). Compared to the results obtained for the reference case in Fig. 12, minor differences are noticed in the overall development of the plastic zone. Including a strain-dependent evolution of the intrinsic permeability in the simulation gives rise to additional hydro-mechanical couplings slightly interfering with the initiation of localisation bands, that tend to grow preferentially in the horizontal direction. However, the total extent of the EDZ remains all in all identical. Permeability variations

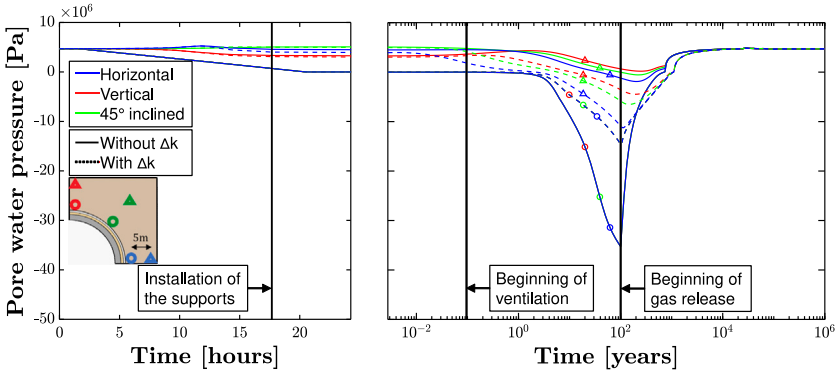

(a) Excavation phase (b) Ventilation and gas migration phases

Fig. 21. Time evolution of pore water pressure during the successive phases of the simulation, considering a permeability evolution with strain.

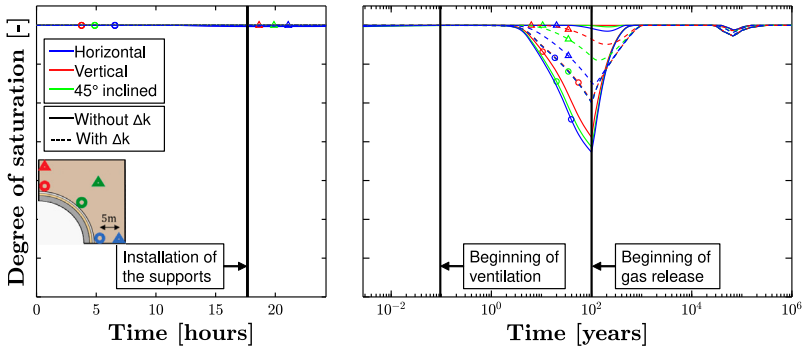

(a) Excavation phase (b) Ventilation and gas migration phases

Fig. 22. Time evolution of water degree of saturation during the successive phases of the simulation, considering a permeability evolution with strain.

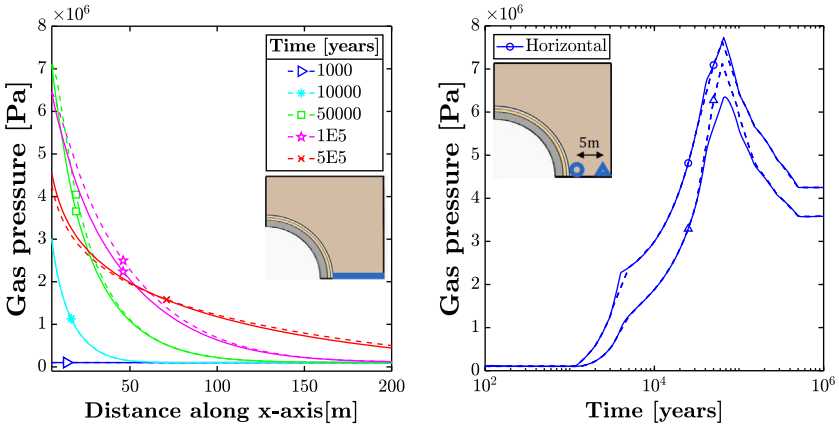

(a) (b)

Fig. 23. Evolution of gas (Hydrogen) pressures (a) over the domain and (b) over time, considering a permeability evolution with strain.

are well visible in the part of this damaged zone which is the closest to the drift wall, and more particularly inside the strain localisation discontinuities where a significant increase of several orders of magnitude is obtained.

A closer look at the distribution of the parallel intrinsic permeability provided in Fig. 20 confirms a global permeability increase of about two orders of magnitude between the initial and final states of excavation, with permeability peaks along the diagonal and horizontal profiles because of the presence of shear bands in these directions. It is worth noting that a symmetrical evolution of the perpendicular intrinsic permeability would be obtained since the strain-dependent isotropic expression (50) conserves the initial directions of anisotropy and the imposed permeability ratio $\frac{k_{w,\parallel}}{k_{w,\perp}} = 3$.

The effect of permeability variation on the ventilation phase can then be investigated through the temporal evolution of the pore water pressure and of the water degree of saturation close to the drift wall which are depicted in Figs. 21 and 22. Due to the fact that the water transfer capacity through the EDZ has increased, the drainage of the

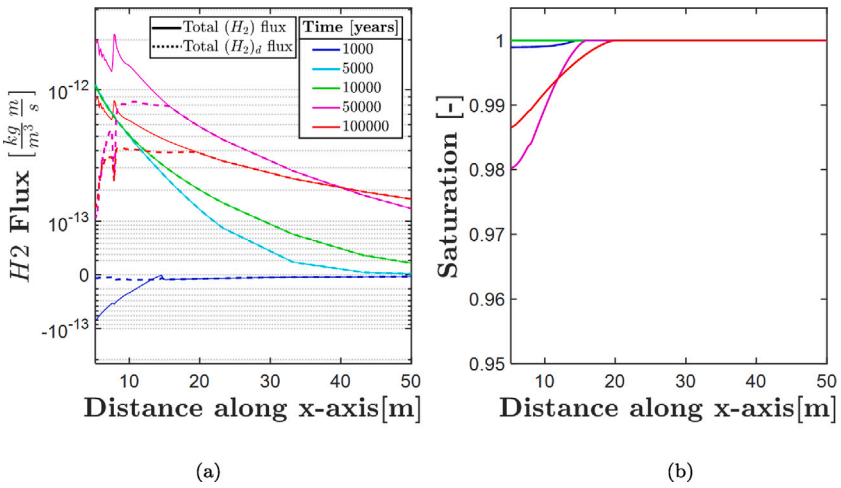

Fig. 24. (a) Comparison between dissolved Hydrogen and total Hydrogen flux (log scale along Y-axis (Webber, 2013)) and (b) corresponding saturation profiles, considering permeability evolution with strain.

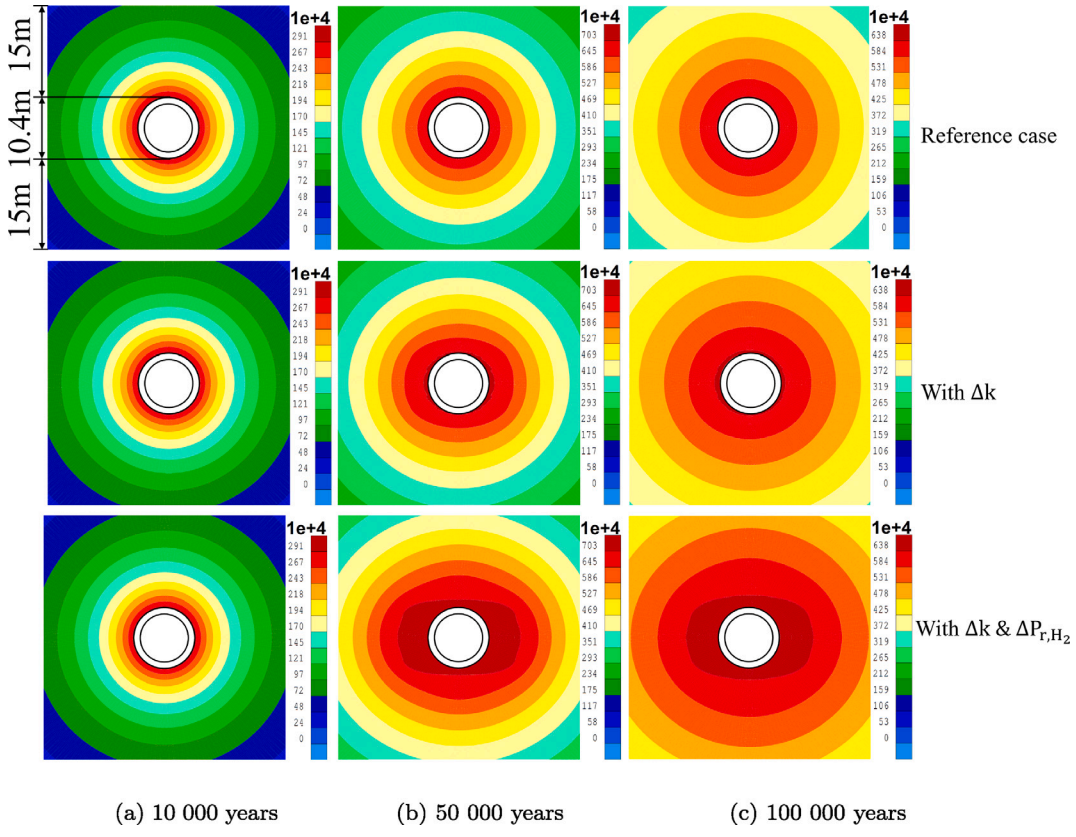

Fig. 25. Evolution of gas (Hydrogen) pressure in the vicinity of the gallery wall, for the reference case and considering the HM couplings.

rock mass becomes more gradual in this zone. The diminution of pore water pressures is slower in the vicinity of the drift due to more water inflows. In parallel the effect of the imposed suction is all the more marked further in the EDZ, especially along the horizontal section given that the plastic zone is more developed in this direction.

With respect to the gas migration phase, the re-establishment of the pore water pressures is also made more progressive, extending the period necessary for the resaturation of the claystone. As a consequence, pore water pressure in the EDZ has not fully returned to its initial state prior to the beginning of gas injection (Fig. 21(b)). From these first observations, it follows that Hydrogen tends to enter the first metres of the rock mass more easily, which is highlighted by a slight horizontal offset of the curves in Fig. 23(a) and by a rise in the maximum gas pressure reached beyond the EDZ in Fig. 23(b). As in the reference case, the analysis of the Hydrogen fluxes shown in Fig. 24 reveals that for the largest amount of Hydrogen, a distinct gas phase appears which desaturates the argillite in the vicinity of the support. The maps of gas pressures in Fig. 25 corroborate these aspects and show that Hydrogen propagates more efficiently in the EDZ. More specifically, preferential flow paths corresponding to the localised shear bands seem to initiate around the drift due to the high increase in permeability within these discontinuities where the deformation is concentrated.

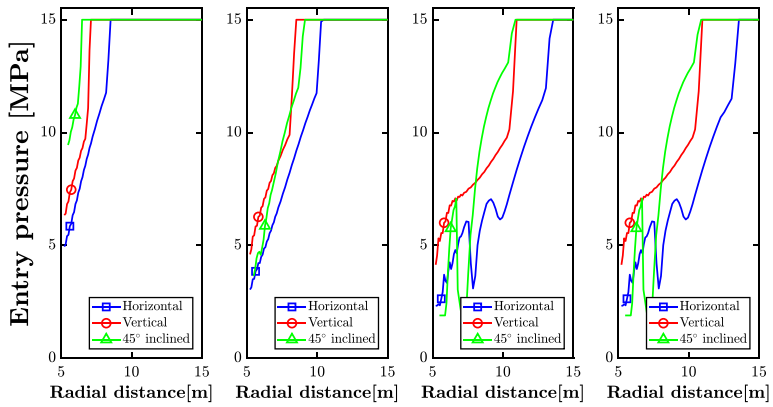

(a) 10h15 (65%) (b) 11h20 (80%) (c) 1 day (100%) (d) 100 years (100%)

Fig. 26. Variation of gas (Hydrogen) entry pressure P_r as a function of the radial distance for different time steps.

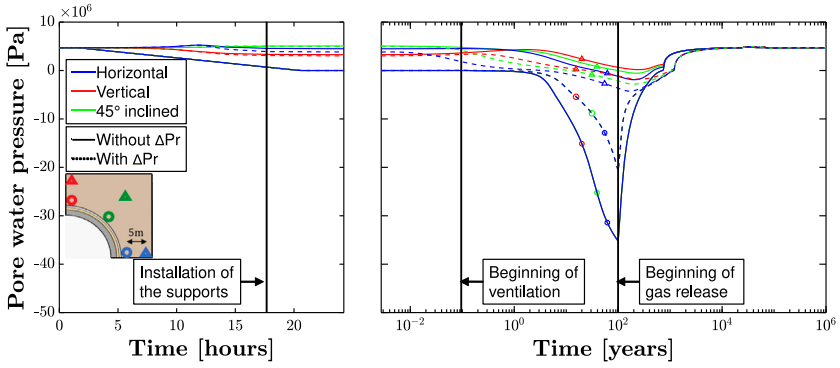

(a) Excavation phase (b) Ventilation and gas migration phases

Fig. 27. Time evolution of pore water pressure during the successive phases of the simulation, considering an evolution of the retention curve with strain.

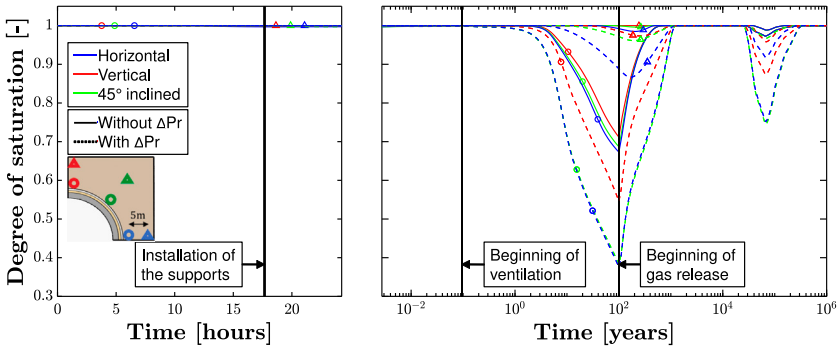

(a) Excavation phase (b) Ventilation and gas migration phases

Fig. 28. Time evolution of water degree of saturation during the successive phases of the simulation, considering an evolution of the retention curve with strain.

5.3. Evolution of the retention curve with the deformations

Next to the increase in the hydraulic permeability with strain, an additional HM mechanism is considered in order to obtain a more faithful representation of the influence of the EDZ on the hydraulic kinetics. This second advanced HM coupling concerns the evolution of the water retention curve with strain (Olivella and Alonso, 2008; Gerard et al., 2012). Indeed, the water retention property of the rock is susceptible to be affected by the modification of the pore network morphology induced by cracking and damage processes. In particular, the increase in pore size following the opening of discontinuities is correlated to the reduction of the gas entry pressure. This feature is integrated into the model thanks to the expression (51) given in Section 4.

The evolution of the entry pressure parameter for the Hydrogen P_r is given in Fig. 26 by the end of the excavation and ventilation phases. These results attest of a global drop in P_r in the EDZ, correlated to the evolution of intrinsic permeability previously observed. As for the evolution of the intrinsic permeability displayed in Fig. 20, the influence of shear bands on P_r is also clearly visible.

Then, the effect of the evolution of the entry pressure on the ventilation phase is investigated through the temporal evolution of the pore water pressure and of the water degree of saturation close to the drift wall, which are depicted in Figs. 27 and 28. The Hydrogen

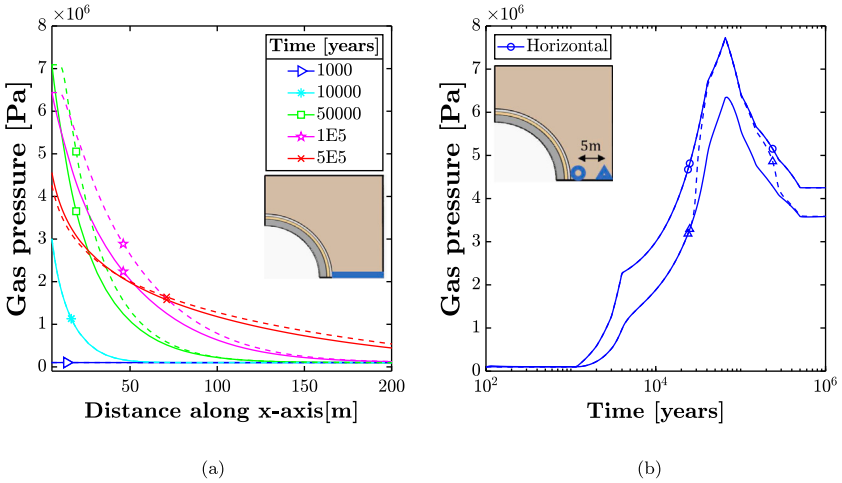

Fig. 29. Evolution of gas (Hydrogen) pressures (a) over the domain and (b) over time, considering an evolution of the retention curve with strain.

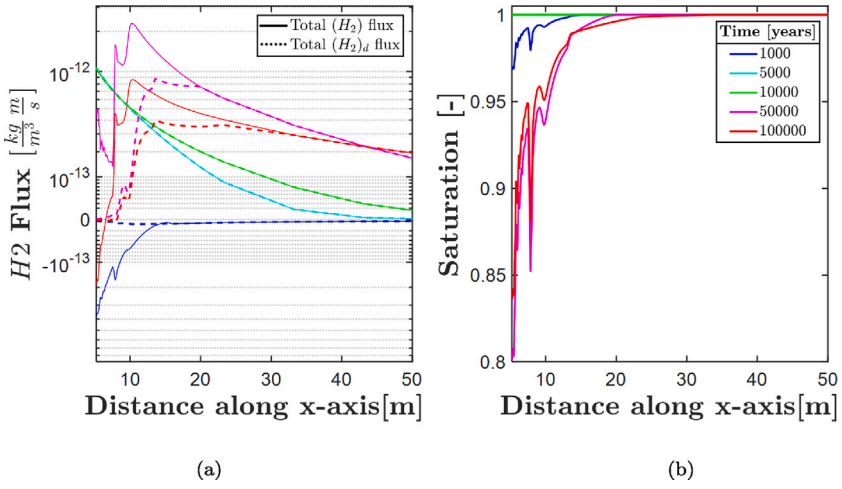

Fig. 30. (a) Comparison between dissolved Hydrogen and total Hydrogen flux (log scale along Y-axis (Webber, 2013)) and (b) corresponding saturation profiles, considering an evolution of the retention curve with strain.

entry pressure reduces significantly after damage, which means that the minimum capillary pressure required to desaturate the rock mass is lowered by the cracking process. Under imposed ventilation, a rapid decrease in the water degree of saturation is thus noted. However, the overall water transfer capacity has been enhanced in the EDZ considering the advanced hydro-mechanical couplings, which leads to a more continuous and gradual drainage of the pore water pressure over the entire EDZ compared to the reference case.

Regarding the gas migration phase, it emerges from Fig. 28(b) that the pore water pressure has almost returned to its initial value, reestablishing a fully saturated state in the EDZ (Fig. 27(b)), prior to the beginning of gas injection. The evolution of the retention curve with the deformations has a clear influence on the Hydrogen migrations. The reduction of Hydrogen entry pressure in the EDZ facilitates even more the penetration of gas into the claystone. Once the Hydrogen pressure reaches and exceeds the water pressure set at 4.7 MPa (in the time window between 3×10^4 and 3×10^5 years), gas progresses in the form of a front through the zone affected by a reduction of the gas entry value (Fig. 29(a)). The maximum gas pressure reached at the limit of the EDZ is then drastically increased as shown in Fig. 29(b). The distinct gas phase that emerges when the largest amounts of Hydrogen are released is clearly discernible in Fig. 30(a). In the EDZ, Hydrogen is no longer dissolved in water but is almost only transferred in the gaseous state, which contributes to a more rapid and important decrease in the degree of water saturation around the drift than in the previous simulations, as reported in Fig. 30(b). All these observations can be further supported with the maps of gas pressures in the vicinity of the drift presented in Fig. 25. The first foreseeable point that can be raised is that Hydrogen propagates easier and faster in that zone compared to the reference case. Moreover, since the cracking process in the EDZ amplifies the desaturation as made explicit in Fig. 28(b), one can notice a uniform and rapid increase in gas pressure across the whole EDZ. This gas front propagation attenuates the preferential flow paths along the localised shear bands highlighted in Section 5.2, as well as band activity reactivation by the end of gas migration phase.

6. Conclusion and outlooks

The present paper is devoted to the numerical analysis of gas migrations in clay materials and their interaction with damaged rock, applied to the specific context of deep geological disposal of nuclear waste. To that end, a second gradient two-phase flow hydro-mechanical (H^2M) model is implemented. This model integrates the second gradient theory to properly reproduce the fractures around underground structures with strain localisation in shear band mode. In order to deal with the mechanisms inherent to gas migrations (Marschall et al., 2005), the model incorporates the features of an extended two-phase flow transfer approach, which allows to reproduce localised flows within shear bands thanks to additional couplings. In particular, the model takes account of specific coupled effects of the mechanical deformations on fluids transport properties like the intrinsic permeability and the retention behaviour. With this numerical tool, this work makes a contribution

to better apprehend the impact of the excavated damaged zone on gas transport.

After the description of the equations used in the finite element code, the modelling of a large-scale storage drift is carried out. The selected case study focuses on a configuration close to the MAVL storage drift drilled in the Callovo-Oxfordian claystone, a low-permeable rock envisaged for deep geological disposal in France. A complete constitutive hydro-mechanical model encompassing viscoplastic effect is employed to reproduce the rock behaviour. The numerical simulation takes place in three phases: gallery excavation on the short term, gallery ventilation in the medium term and Hydrogen production and migration in the long term.

Three distinct configurations are investigated and compared with respect to desaturation and fluids transfer in the excavation damaged zone. In the reference hydro-mechanical simulation the effect of mechanics on the hydraulic properties of the rock is not taken into account. The second modelling assumes an evolution of the intrinsic permeability according to a strain-dependent relation while the last simulation includes an additional hydro-mechanical coupling by taking the influence of cracking and damage on the water retention property of the material into account.

The numerical results provides first a representative characterisation of rock fracturing within the EDZ during the excavation phase. An important rock desaturation is furthermore noted in the fractured zone surrounding the drift during the pore water drainage imposed by the ventilation phase. During the phase of gas injection, it appears that dissolved gas is not sufficient enough to transport Hydrogen under large production of gas. This leads to the creation of a gaseous phase along with the desaturation of the first metres of the rock mass. Concerning the hydro-mechanical couplings that take place in the damaged zone, a permeability increase of several orders of magnitude can be obtained within the shear bands by imposing permeability variations with the localisation effect. This way, faster Hydrogen propagation is observed in the EDZ with evidence of preferential pathway initiation for gas flows within the bands. Introducing the second hydro-mechanical effect in the simulation, which couples water retention property of the rock and damage process, significantly amplifies the desaturation of the rock mass. It consequently results in an even more rapid progression of Hydrogen across the EDZ in the form of a gaseous front. It is worth noting that these coupled effects are globally limited to the EDZ close to the drift wall and tend to attenuate deeper in the rock mass. In the end, the conclusion of the performed analysis demonstrates the non-negligible impact of the hydro-mechanical couplings inherent to the EDZ on gas migrations. Incorporate these couplings in the modelling should therefore lead to more realistic and accurate predictions of the long-term behaviour of a deep geological disposal.

Of course, the elaborated numerical model can still be improved which opens new perspectives of development on the question of gas transfers in clay materials. In particular, the model could be extended to short-term thermal effects in order to study how the generated heat could induce water overpressures and affect the favourable properties of the clay host rock, especially its transport characteristics. With respect to the topic of nuclear waste disposal, the proposed numerical approach could be extended to other host rock formations adopted in Europe, which will require some adaptation of the couplings to the considered material. Moreover, among the extra coupled processes prone to occur in clay materials, healing of the rock is a physical mechanism that would result in the closure of fractures along with simultaneous reduction in permeability and fluids transport. This paper especially focuses on gas transfers through the excavation damaged zone around the storage drift which are driven by hydraulic properties modification induced by fracturation. In parallel, gas migrations in the surrounding sound rock layer is another issue to investigate. In this case, transfers are mainly governed by the rock structure at a micro-level which would require the recourse to more complex computation strategies, e.g. multi-scale model based on the FE^2 method.

Declaration of competing interest

The authors declare that they have no known competing financial interests or personal relationships that could have appeared to influence the work reported in this paper.

Acknowledgements

The authors are grateful for financial supports from EURAD, the European Joint Programme on Radioactive Waste Management (under grant agreement No 847593), and from ANDRA, the French national radioactive waste management agency.

Appendix. Linearisation of the field equations

The linearisation of the field Eqs. (6), (7), (9) and (10) of the local second gradient model for multiphasic medium, leading to the linear auxiliary problem (26) is detailed hereafter.

Since this system of highly non-linear relations is *a priori* not numerically satisfied at any instant t, an iterative procedure of Newton–Raphson type is employed. To this end, time discretisation into finite time steps Δt is prerequisite, which leads to two configurations. One configuration Ω^t is assumed to be known and in equilibrium with the boundary conditions at a given time t of the loading, and the other configuration Ω^τ is not at equilibrium at a time $\tau = t + \Delta t$. Following the work of Borja and Alarcón (1995), the objective is to find a new configuration in equilibrium at the end of the time step. Accordingly, a first guess of this new configuration, which is close to the solution but not at equilibrium is proposed and denoted as $\Omega^{\tau 1}$. Both configurations at time t and $\tau 1$ are assumed to be known and non-equilibrium forces, i.e. residuals $\Delta_1^{\tau 1}$, $\Delta_2^{\tau 1}$, $\Delta_3^{\tau 1}$, $\Delta_4^{\tau 1}$, are respectively defined in the four governing equations:

$$\int_{\Omega^{\tau 1}} \left(\sigma_{ij}^{\tau 1} \frac{\partial u_i^\star}{\partial x_j^{\tau 1}} + \Sigma_{ijk}^{\tau 1} \frac{\partial v_{ij}^\star}{\partial x_k^{\tau 1}} \right) d\Omega^{\tau 1} - \int_{\Omega^{\tau 1}} \lambda_{ij}^{\tau 1} \left(\frac{\partial u_i^\star}{\partial x_j^{\tau 1}} - v_{ij}^\star \right) d\Omega^{\tau 1} - \int_{\Omega^{\tau 1}} \rho_{mix}^{\tau 1} g_i u_i^\star \, d\Omega^{\tau 1} - \int_{\Gamma_\sigma^{\tau 1}} \left(\bar{t}_i^{\tau 1} u_i^\star + \bar{T}_i^{\tau 1} v_{ik}^\star n_k^{\tau 1} \right) d\Gamma^{\tau 1} = \Delta_1^{\tau 1} \tag{A.1}$$

$$\int_{\Omega^{\tau 1}} \lambda_{ij}^\star \left(\frac{\partial u_i^{\tau 1}}{\partial x_j^{\tau 1}} - v_{ij}^{\tau 1} \right) d\Omega^{\tau 1} = \Delta_2^{\tau 1} \tag{A.2}$$

$$\int_{\Omega^{\tau 1}} \left[\dot{M}_w^{\tau 1} p_w^\star + \dot{M}_v^{\tau 1} p_w^\star - f_{w,i}^{\tau 1} \frac{\partial p_w^\star}{\partial x_i^{\tau 1}} - f_{v,i}^{\tau 1} \frac{\partial p_w^\star}{\partial x_i^{\tau 1}} \right] d\Omega^{\tau 1} - \int_{\Omega^{\tau 1}} Q_w^{\tau 1} p_w^\star d\Omega^{\tau 1} + \int_{\Gamma^{\tau 1}} \bar{q}_w^{\tau 1} p_w^\star d\Gamma^{\tau 1} = \Delta_3^{\tau 1} \tag{A.3}$$

$$\int_{\Omega^{\tau 1}} \left[\dot{M}_{H_2}^{\tau 1} p_g^\star + \dot{M}_{H_2^d}^{\tau 1} p_g^\star - f_{H_2,i}^{\tau 1} \frac{\partial p_g^\star}{\partial x_i^{\tau 1}} - f_{H_2^d,i}^{\tau 1} \frac{\partial p_g^\star}{\partial x_i^{\tau 1}} \right] d\Omega^{\tau 1} - \int_{\Omega^{\tau 1}} Q_{H_2}^{\tau 1} p_g^\star d\Omega^{\tau 1} + \int_{\Gamma^{\tau 1}} \bar{q}_g^{\tau 1} p_g^\star d\Gamma^{\tau 1} = \Delta_4^{\tau 1} \tag{A.4}$$

The aim is then to define another configuration denoted $\Omega^{\tau 2}$, close to $\Omega^{\tau 1}$, for which the non-equilibrium forces vanish. Rewriting the field equations related to $\Omega^{\tau 2}$ in configuration $\Omega^{\tau 1}$ (using the Jacobian transformation), assuming in addition that g_i, $\bar{t}_i$, $\bar{q}_w$, $\bar{q}_g$, Q_w, Q_{H_2} are independent of the different unknown fields, and that $\bar{T}_i$ vanishes, and

subtracting after all the balance equations for the two configurations yields:

$$\begin{aligned}&\int_{\Omega^{\tau 1}} \frac{\partial u_i^\star}{\partial x_l^{\tau 1}}\left(\sigma_{ij}^{\tau 2}\frac{\partial x_l^{\tau 1}}{\partial x_j^{\tau 2}}detF-\sigma_{il}^{\tau 1}\right)\\&\quad+\frac{\partial v_{ij}^\star}{\partial x_l^{\tau 1}}\left(\Sigma_{ijk}^{\tau 2}\frac{\partial x_l^{\tau 1}}{\partial x_k^{\tau 2}}detF-\Sigma_{ijl}^{\tau 1}\right)d\Omega^{\tau 1}\\&\quad-\frac{\partial u_i^\star}{\partial x_l^{\tau 1}}\left(\lambda_{ij}^{\tau 2}\frac{\partial x_l^{\tau 1}}{\partial x_j^{\tau 2}}detF-\lambda_{il}^{\tau 1}\right)\\&\quad-v_{ij}^\star\left(\lambda_{ij}^{\tau 2}detF-\lambda_{ij}^{\tau 1}\right)\\&\quad-u_i^\star\left(\rho_{mix}^{\tau 2}detF-\rho_{mix}^{\tau 1}\right)g_i d\Omega^{\tau 1}=-\Delta_1^{\tau 1}\end{aligned}\tag{A.5}$$

$$\begin{aligned}&\int_{\Omega^{\tau 1}}\lambda_{ij}^\star\left(\frac{\partial u_i^{\tau 2}}{\partial x_k^{\tau 1}}\frac{\partial x_k^{\tau 1}}{\partial x_j^{\tau 2}}detF-\frac{\partial u_i^{\tau 1}}{\partial x_1^{\tau 1}}\right)\\&\quad-\lambda_{ij}^\star\left(v_{ij}^{\tau 2}detF-v_{ij}^{\tau 1}\right)d\Omega^{\tau 1}=-\Delta_2^{\tau 1}\end{aligned}\tag{A.6}$$

$$\begin{aligned}&\int_{\Omega^{\tau 1}} p_w^\star\left(\dot{M}_w^{\tau 2}detF+\dot{M}_v^{\tau 2}detF-\dot{M}_w^{\tau 1}-\dot{M}_v^{\tau 1}\right)\\&-\frac{\partial p_w^\star}{\partial x_k^{\tau 1}}\left(f_{w,i}^{\tau 2}\frac{\partial x_k^{\tau 1}}{\partial x_j^{\tau 2}}detF+f_{v,i}^{\tau 2}\frac{\partial x_k^{\tau 1}}{\partial x_j^{\tau 2}}detF-f_{w,k}^{\tau 1}-f_{v,k}^{\tau 1}\right)d\Omega^{\tau 1}=-\Delta_3^{\tau 1}\end{aligned}\tag{A.7}$$

$$\begin{aligned}&\int_{\Omega^{\tau 1}} p_g^\star\left(\dot{M}_{H_2}^{\tau 2}detF+\dot{M}_{dH_2}^{\tau 2}detF-\dot{M}_{H_2}^{\tau 1}-\dot{M}_{dH_2}^{\tau 1}\right)\\&-\frac{\partial p_g^\star}{\partial x_k^{\tau 1}}\left(f_{H_2,i}^{\tau 2}\frac{\partial x_k^{\tau 1}}{\partial x_j^{\tau 2}}detF\right.\\&\left.+f_{H_2^d,i}^{\tau 2}\frac{\partial x_k^{\tau 1}}{\partial x_j^{\tau 2}}detF-f_{H_2,k}^{\tau 1}-f_{H_2^d,k}^{\tau 1}\right)d\Omega^{\tau 1}=-\Delta_4^{\tau 1}\end{aligned}\tag{A.8}$$

where $\frac{\partial x_i^{\tau 2}}{\partial x_j^{\tau 1}}$ is the Jacobian matrix of the transformation between the two configurations, and $detF=\left|\frac{\partial x_i^{\tau 2}}{\partial x_j^{\tau 1}}\right|$ is the Jacobian determinant.

By making the two configurations tend towards each other, which leads to the limit $\tau 2=\tau 1$ the variations of the quantities of the problem can be defined as:

$$du_i^t=x_i^{\tau 2}-x_i^{\tau 1}\tag{A.9}$$

$$dv_{ij}^t=v_{ij}^{\tau 2}-v_{ij}^{\tau 1}\tag{A.10}$$

$$d\lambda_{ij}^t=\lambda_{ij}^{\tau 2}-\lambda_{ij}^{\tau 1}\tag{A.11}$$

$$d\sigma_{ij}^t=\sigma_{ij}^{\tau 2}-\sigma_{ij}^{\tau 1}=d\sigma_{ij}'^t+bS_r^{w,t}dp_w^t\delta_{ij}+b(1-S_r^{w,t})dp_g^t\delta_{ij}\tag{A.12}$$

$$d\Sigma_{ijk}^t=\Sigma_{ijk}^{\tau 2}-\Sigma_{ijk}^{\tau 1}\tag{A.13}$$

$$d\phi^t=\phi^{\tau 2}-\phi^{\tau 1}=(b-\phi^t)\left[\frac{S_r^{w,t}}{K_s}dp_w^t+\frac{1-S_r^{w,t}}{K_s}dp_g^t+d\varepsilon_v^t\right]\tag{A.14}$$

$$d\rho_w^t=\rho_w^{\tau 2}-\rho_w^{\tau 1}=\rho_w^t\frac{dp_w^t}{\chi_w}\tag{A.15}$$

$$d\rho_g^t=\rho_g^{\tau 2}-\rho_g^{\tau 1}=\frac{m_{H_2}}{RT}p_{H_2}^t+\frac{m_v}{RT}p_v^t\tag{A.16}$$

$$d\rho_s^t=\rho_s^{\tau 2}-\rho_s^{\tau 1}=\frac{(b-\phi^t)(S_r^{w,t}dp_w^t+(1-S_r^{w,t})dp_g^t)+d\sigma'^t}{(1-\phi^t)K_s}\tag{A.17}$$

$$d\varepsilon_v^t=\frac{d\Omega^t}{\Omega^t}=\frac{\partial du_i^t}{\partial x_i^t}\tag{A.18}$$

Taking these variations into account and using a Taylor expansion of Eqs. (A.5) to (A.8) with discarding terms of degree greater than one gives, after some algebra, a linearised system of field equations (see Chambon et al. (2001b), Chambon and Moullet (2004) and Collin et al. (2006) for more detailed analytical developments). This allows to assess the corrections of the unknown fields to be added to the respective current values to obtain a new configuration closer to a well-balanced configuration.

References

Aifantis, E.C., 1984. On the microstructural origin of certain inelastic models. J. Eng. Mater. Technol. 106 (4), 326–330.

Amadei, B., 1983. Rock Anisotropy and the Theory of Stress Measurements. In: Lecture Notes in Engineering Series, vol. 2, Springer-V edition, New-York, The United States.

Andra, 2016. Analyse de l'Interaction (Thermo-)Hydro-Mécanique des Alvéoles MAVL - Approche Milieu Continu. Technical report, Agence natioanle pour la gestion des déchets radioactifs, Châtenay-Malabry, France, p. 34.

Argilaga, A., Collin, F., Lacarrière, L., Charlier, R., Armand, G., Cerfontaine, B., 2019. Modelling of short-term interactions between concrete support and the excavated damage zone around galleries drilled in callovo–oxfordian claystone. Int. J. Civ. Eng. 17 (1).

Armand, G., Leveau, F., Nussbaum, C., De La Vaissiere, R., Noiret, A., Jaeggi, D., Landrein, P., Righini, C., 2014. Geometry and properties of the excavation-induced fractures at the Meuse/Haute-Marne URL drifts. Rock Mech. Rock Eng. 47 (1), 21–41.

Ausness, R.C., 1979. High-level radioactive waste management : The nuclear dilemma. Wis. Law Rev. 707.

Autio, J., Gribi, P., Johnson, L., Marschall, P., 2006. Effect of excavation damaged zone on gas migration in a KBS-3H type repository at Olkiluoto. Phys. Chem. Earth 31 (10–14), 649–653.

Bažant, Z.P., Belytschko, T.B., 1985. Wave propagation in a strain-softening bar: Exact solution. J. Eng. Mech. 111 (3), 381–389.

Bazant, Z.P., Belytschko, T.B., Chang, T.-P., 1984. Continuum theory for strain-softening. J. Eng. Mech. 110 (12), 1666–1692.

Bernaud, D., Rousset, G., 1992. La « nouvelle méthode implicite » pour l'étude du dimensionnement des tunnels. Rev. Fr. Géotech. (60), 5–26.

Biot, M.A., 1941. General theory for three-dimensional consolidation. J. Appl. Phys. 12 (2), 155–164.

Bishop, A.W., 1959. The principle of effective stress. Tek. Ukebl. 39, 859–863.

Borja, R.I., Alarcón, E., 1995. A mathematical framework for finite strain elastoplastic consolidation Part 1: Balance laws, variational formulation, and linearization. Comput. Methods Appl. Mech. Engrg. 122 (1–2), 145–171.

Bredehoeft, J.D., England, A.W., Steward, D.B., Trask, N.J., Winograd, I.J., 1978. Geologic disposal of high-level radioactive wastes, earth-science perspectives. In: U.S. Geological Survey Circular 779. Technical report, U.S. Geological Survey, p. 15.

Chambon, R., Caillerie, D., El Hassan, N., 1998. One-dimensional localisation studied with a second grade model. Eur. J. Mech. A/Solids 17 (4), 637–656.

Chambon, R., Caillerie, D., Matsuchima, T., 2001a. Plastic continuum with microstructure, local second gradient theories for geomaterials: Localization studies. Int. J. Solids Struct. 38 (46–47), 8503–8527.

Chambon, R., Crochepeyre, S., Charlier, R., 2001b. An algorithm and a method to search bifurcation points in non-linear problems. Internat. J. Numer. Methods Engrg. 51 (3), 315–332.

Chambon, R., Moullet, J.C., 2004. Uniqueness studies in boundary value problems involving some second gradient models. Comput. Methods Appl. Mech. Engrg. 193 (27–29), 2771–2796.

Charlier, R., 1987. Approche Unifiée de Quelques Problèmes Non Linéaires de Mécanique des Milieux Continus par la Méthode des Éléments Finis (Grandes Déformations des Métaux et des Sols, Contact Unilatéral de Solides, Conduction Thermique et Écoulements en Milieux Poreux). (Ph.D. thesis). Faculty of Applied Sciences, University of Liège, Belgium, p. 301.

Charlier, R., Collin, F., Pardoen, B., Talandier, J., Radu, J.-P., Gerard, P., 2013. An unsaturated hydro-mechanical modelling of two in-situ experiments in Callovo-Oxfordian argillite. Eng. Geol. 165, 46–63.

Cheng, A.H.-D., 1997. Material coefficients of anisotropic poroelasticity. Int. J. Rock Mech. Min. Sci. 34 (2), 199–205.

Clapeyron, E., 1834. Mémoire sur la Puissance Motrice de la Chaleur. J. Éc. Polytech. 23, 153–191.

Collin, F., 2003. Couplages Thermo-Hydro-Mécaniques dans les Sols et les Roches Tendres Partiellement Saturés (thésis / mémoire). Faculty of Applied Sciences, University of Liège, Belgium, p. 332.

Collin, F., Caillerie, D., Chambon, R., 2009. Analytical solutions for the thick-walled cylinder problem modeled with an isotropic elastic second gradient constitutive equation. Int. J. Solids Struct. 46 (22–23), 3927–3937.

Collin, F., Chambon, R., Charlier, R., 2006. A finite element method for poro mechanical modelling of geotechnical problems using local second gradient models. Internat. J. Numer. Methods Engrg. 65 (11), 1749–1772.
Cosserat, E., Cosserat, F., 1909. Théorie des Corps Déformables. A Hermann edition, Paris, France, p. 250.
Coussy, O., 1995. Mechanics of Porous Continua. Chichester., p. 472.
Coussy, O., 2004. Poromechanics. London, England, p. 315.
Dalton, J., 1802. Essay IV. On the expansion of elastic fluids by heat. Mem. Lit. Philos. Soc. Manch. 5 (2), 595–602.
Darcy, H., 1856. In: Dalmont, V. (Ed.), Les Fontaines Publiques de la Ville de Dijon. Librairie des Corps Impériaux des Ponts et Chaussées et des Mines, Paris, France, p. 647.
De Borst, R., Mühlhaus, H.-B., 1992. Gradient-dependent plasticity: Formulation and algorithmic aspects. Internat. J. Numer. Methods Engrg. 35 (3), 521–539.
De Borst, R., Sluys, L.J., Mühlhaus, H.-B., Pamin, J., 1993. Fundamental issues in finite element analyses of localization of deformation. Eng. Comput. 10 (2), 99–121.
Desrues, J., Viggiani, G., 2004. Strain localization in sand: An overview of the experimental results obtained in Grenoble using stereophotogrammetry. Int. J. Numer. Anal. Methods Geomech. 28 (4), 279–321.
Detournay, E., Cheng, A., 1993. Fundamentals of poroelasticity. In: Comprehensive Rock Engineering: Principles, Practice and Projects. Vol. 2. Pergamon Press, Oxford, pp. 113–171, chapter 5.
Ehlers, W., Volk, W., 1998. On theoretical and numerical methods in the theory of porous media based on polar and non-polar elasto-plastic solid materials. Int. J. Solids Struct. 35 (34–35), 4597–4617.
European_Commission, 2005. Ventilation Experiment in Opalinus Clay for the Disposal of Radioactive Waste in Underground Repositories (Project Funded By the European Community under the 'EURATOM' Programme 1998–2002 under Contract No. FIKWCT-2001-00126). Technical Report. Nuclear Sc edition, Luxembourg, p. 54.
Ewing, R.C., Whittleston, R.A., Yardley, B.W.D., 2016. Geological disposal of nuclear waste: A primer. Elements 12 (4), 233–237.
Fick, A., 1855. Über diffusion [Translated: On liquid diffusion]. Poggendorff's Ann. Phys. Chem. 170 (1), 59–86.
Finno, R.J., Wendell, W.H., Mooney, M.A., Viggiani, G., 1996. Strain localization and undrained steady state of sand. J. Geotech. Geoenviron. Eng. 122 (6), 462–473.
Gallé, C., 2000. Gas breakthrough pressure in compacted Fo-Ca clay and interfacial gas overpressure in waste disposal context. Appl. Clay Sci. 17 (1–2), 85–97.
Gerard, P., 2011. Impact des Transferts de Gaz sur le Comportement Poro-Mécanique des Matériaux Argileux Thèse Présentée Par (Thésis présentée par). University of Liège, p. 301.
Gerard, P., Charlier, R., Su, K., Duveau, G., Giot, R., Chavant, C., Collin, F., 2008. Numerical modelling of coupled mechanics and gas tansfer around radioactive waste in long-term storage. J. Theoret. Appl. Mech. 38, 25–44.
Gerard, P., Harrington, J., Charlier, R., Collin, F., 2012. Hydro-mechanical modelling of the development of preferential gas pathways in claystone. In: Unsaturated Soils: Research and Applications. pp. 175–180.
Gerard, P., Harrington, J., Charlier, R., Collin, F., 2014. Modelling of localised gas preferential pathways in claystone. Int. J. Rock Mech. Min. Sci. 67, 104–114.
Germain, P., 1973. The method of virtual power in continuum mechanics. Part 2 microstructure. Soc. Ind. Appl. Math. 25 (3), 556–575.
Hill, R.H., 1958. General stability theory of uniqueness and stability in elasto-plastic solids. J. Mech. Phys. Solids 6, 239–249.
Hill, R., Hutchinson, J.W., 1975. Bifurcation phenomena in the plane tension test. J. Mech. Phys. Solids 23 (4–5), 239–264.
IAEA, 2003. Scientific and technical basis for the geological disposal of radioactive wastes. Technical Report 4, International Atomic Energy Agency, New-York, p. 90.
Jia, Y., Bian, H.B., Duveau, G., Su, K., Shao, J.F., 2008. Hydromechanical modelling of shaft excavation in Meuse/Haute-Marne laboratory. Phys. Chem. Earth 33 (SUPPL. 1), 422–435.
Jouan, G., Kotronis, P., Caillerie, D., Collin, F., 2022. A second gradient cohesive element for mode I crack propagation. Finite Elem. Anal. Des. 204 (30), 103732.
Lekhnitskii, S.G., 1963. Theory of Elasticity of an Anisotropic Elastic Body. Holden-Day edition, San Fransisco, The USA, p. 793.
Levasseur, S., Collin, F., Charlier, R., Kondo, D., 2013. A micro-macro approach of permeability evolution in rocks excavation damaged zones. Comput. Geotech. 49, 245–252.
Lewis, R.W., Schrefler, B.A., 2000. The Finite Element Method in the Static and Dynamic Deformation and Consolidation of Porous Media. John Wiley & Sons, New-York, The United States, p. 477.
Li, X., et al., 2007. In: Li, X. (Ed.), TIMODAZ: Thermal Impact on the Damaged Zone Around a Radioactive Waste Disposal in Clay Host Rocks. Deliverable 2. State of the Art on THMC. Technical report, Euratom European Project, p. 203.
Lisjak, A., Garitte, B., Grasselli, G., Müller, H.R., Vietor, T., 2015. The excavation of a circular tunnel in a bedded argillaceous rock (Opalinus Clay): Short-term rock mass response and FDEM numerical analysis. Tunn. Undergr. Space Technol. 45 (February 2019), 227–248.
Lyapunov, A.M., 1892. The General Problem of the Stability of Motion. Taylor & Francis (1992), translated edition.
Marschall, P., Horseman, S., Gimmi, T., 2005. Characterisation of gas transport properties of the opalinus clay, a potential host rock formation for radioactive waste disposal. Oil Gas Sci. Technol. – Rev. IFP 60 (1), 121–139.
Matsushima, T., Chambon, R., Caillerie, D., 2002. Large strain finite element analysis of a local second gradient model: Application to localization. Internat. J. Numer. Methods Engrg. 54 (4), 499–521.
Mindlin, R.D., 1964. Micro-structure in linear elasticity. Arch. Ration. Mech. Anal. 16 (1), 51–78.
Mindlin, R.D., 1965. Second gradient of strain and surface-tension in linear elasticity. Int. J. Solids Struct. 1 (4), 417–438.
Mualem, J., 1976. A new model for predicting the hydraulic conductivity of unsaturated porous media. Water Resour. Res. 12 (3), 513–522.
NEA Expert Group, 1986. Shallow Land Disposal of Radioactive Waste: Refrence Levels for the Acceptance of Long-lived Radionuclides. Technical report, Nuclear Energy Agency and Economic Cooperation and development, Paris, p. 76.
Olivella, S., Alonso, E.E., 2008. Gas flow through clay barriers. Géotechnique 58 (3), 157–176.
Ortiz, L., Volckaert, G., Mallants, D., 2002. Gas generation and migration in Boom Clay, a potential host rock formation for nuclear waste storage. Eng. Geol. 64 (2–3), 287–296.
Pardoen, B., Collin, F., 2017. Modelling the influence of strain localisation and viscosity on the behaviour of underground drifts drilled in claystone. Comput. Geotech. 85, 351–367.
Pardoen, B., Levasseur, S., Collin, F., 2014. Excavation damaged zone modelling including hydraulic permeability evolution in unsaturated argilaceous rock. In: Unsaturated Soils: Research and Applications - Proceedings of the 6th International Conference on Unsaturated Soils, UNSAT 2014, 2(Desrues). pp. 1387–1393.
Pardoen, B., Levasseur, S., Collin, F., 2015a. Using local second gradient model and shear strain localisation to model the excavation damaged zone in unsaturated claystone. Rock Mech. Rock Eng. 48 (2), 691–714.
Pardoen, B., Seyedi, D.M., Collin, F., 2015b. Shear banding modelling in cross-anisotropic rocks. Int. J. Solids Struct. 72, 63–87.
Pardoen, B., Talandier, J., Collin, F., 2016. Permeability evolution and water transfer in the excavation damaged zone of a ventilated gallery. Int. J. Rock Mech. Min. Sci. 85, 192–208.
Peerlings, R.H.J., De Borst, R., Brekelmans, W.A.M., De Vree, J.H.P., 1996. Gradient enhanced damage for quasi-brittle materials. Internat. J. Numer. Methods Engrg. 39 (19), 3391–3403.
Pellet, F., Roosefid, M., Deleruyelle, F., 2009. On the 3D numerical modelling of the time-dependent development of the damage zone around underground galleries during and after excavation. Tunn. Undergr. Space Technol. 24 (6), 665–674.
Pietruszczak, S.T., Mróz, Z., 1981. Finite element analysis of deformation of strain-softening materials. Internat. J. Numer. Methods Engrg. 17 (3), 327–334.
Pijaudier-Cabot, G., Bazant, Z.P., 1987. Nonlocal damage theory. J. Eng. Mech. 113 (10), 1512–1533.
Plassart, R., Fernandes, R., Giraud, A., Hoxha, D., Laigle, F., 2013. Hydromechanical modelling of an excavation in an underground research laboratory with an elastoviscoplastic behaviour law and regularization by second gradient of dilation. Int. J. Rock Mech. Min. Sci. 58, 23–33.
Rattez, H., Stefanou, I., Sulem, J., Veveakis, M., Poulet, T., 2018. Numerical analysis of strain localization in rocks with thermo-hydro-mechanical couplings using cosserat continuum. Rock Mech. Rock Eng. 51 (10), 3295–3311.
Rice, J.R., 1976. Localization of plastic deformation. In: Koiter, W.T. (Ed.), Theoretical and Applied Mechanics, Vol. 1. North-Holland Publishing Company, pp. 207–220.
Rodwell, W.R., Harris, A.W., Horseman, S.T., Lalieux, P., Müller, W., Ortiz Amaya, L., Pruess, K., 1999. Gas Migration and Two-Phase Flow through Engineered and Geological Barriers for a Deep Repository for Radioctive Waste. A Joint EC/NEA Status Report. Technical report, European Commission, Brussels, Belgium, p. 429.
Rutqvist, J., Bäckström, A., Chijimatsu, M., Feng, X.T., Pan, P.Z., Hudson, J., Jing, L., Kobayashi, A., Koyama, T., Lee, H.S., Huang, X.H., Rinne, M., Shen, B., 2009. A multiple-code simulation study of the long-term EDZ evolution of geological nuclear waste repositories. Environ. Geol. 57 (6), 1313–1324.
Sentís, M.L., 2014. Two-phase flow modeling with TOUGH2-MP of a deep geological repository within the first benchmark of the FORGE project. Nucl. Technol. 187 (2), 117–130.
Shao, J.F., Zhu, Q.Z., Su, K., 2003. Modeling of creep in rock materials in terms of material degradation. Comput. Geotech. 30 (7), 549–555.
Sieffert, Y., Buzzi, O., Collin, F., 2014. Numerical study of shear band instability and effect of cavitation on the response of a specimen under undrained biaxial loading. Int. J. Solids Struct. 51 (9), 1686–1696.
Sieffert, Y., Marinelli, F., Chambon, R., 2011. Local second gradient models for thermo-hydro-mechanical coupling in rock like materials. In: Bonelli, S., Dascalu, C., Nicot, F. (Eds.), Advances in Bifurcation and Degradation in Geomaterials. Proceedings of the 9th International Workshop on Bifurcation and Degradation in Geomaterials.. pp. 219–226.

Talandier, J., 2005. La Production et le Transfert de Gaz Dans un Stockage et Dans la Couche du Callovo-Oxfordien - Lien Avec le Transitoire Hydraulique - Site de Meuse / Haute-Marne. Rapport Andra n° C.NT.ASCM.03.0042. Technical report, Andra.

Toupin, R.A., 1962. Elastic materials with couple stress. Arch. Ration. Mech. Anal. 11 (1), 385–414.

Triantafyllidis, N., 1980. Bifurcation phenomena in pure bending. J. Mech. Phys. Solids 28 (3–4), 221–245.

Tsang, C.F., Bernier, F., Davies, C., 2005. Geohydromechanical processes in the Excavation Damaged Zone in crystalline rock, rock salt, and indurated and plastic clays - In the context of radioactive waste disposal. Int. J. Rock Mech. Min. Sci. 42 (1), 109–125.

Van Eekelen, H.A.M., 1980. Isotropic yield surfaces in three dimensions for use in soil mechanics. Int. J. Numer. Anal. Methods Geomech. 4 (1), 89–101.

Van Genuchten, M.T., 1980. Predicting the hydraulic conductivity of unsaturated soils. Soil Sci. Soc. Am. J. 44 (5), 892–898.

Vardoulakis, I., Goldscheider, M., Gudehus, G., 1978. Formation of shear bands in sand bodies as a bifurcation problem. Int. J. Numer. Anal. Methods Geomech. 2 (2), 99–128.

Volckaert, G., Ortiz, L., Canniere, P.D., Put, M., Horseman, S.T., Harrington, J.F., Fioravante, V., Impey, M., 1995. MEGAS: Modelling and Experiments on GAS Migration in Repository Host Rocks. Final Report Phase 1. Technical report, Eur. Comm., [Rep.] EUR 16235 EN, p. 464.

Webber, J.B.W., 2013. A bi-symmetric log transformation for wide-range data. Meas. Sci. Technol. 24 (2).

Xue, Y., Dang, F., Shi, F., Li, R., Cao, Z., 2018. Evaluation of gas migration and rock damage characteristics for underground nuclear waste storage based on a coupled model. Sci. Technol. Nucl. Install. 2018, 1–11.

Yu, L., Weetjens, E., Perko, J., Mallants, D., 2011. Comparison of numerical tools through thermo-hydro-gas transport modeling for a geological repository in boom clay. Nucl. Technol. 174 (3), 411–423.

Zbib, H.M., Aifantis, E.C., 1988. On the localization and postlocalization behavior of plastic deformation. Part I. On the initiation of shear bands. Part II. On the evolution and thickness of shear bands. In: Aifantis, et al. (Eds.), Res Mechanica, Vol. 23. Special Issue on Material Instabilities, pp. 261–277; 279–292.

Zervos, A., Papanastasiou, P., Vardoulakis, I., 2001. Modelling of localisation and scale effect in thick-walled cylinders with gradient elastoplasticity. Int. J. Solids Struct. 38, 5081–5095.

Zhou, H., Jia, Y., Shao, J.F., 2008. A unified elastic–plastic and viscoplastic damage model for quasi-brittle rocks. Int. J. Rock Mech. Min. Sci. 45 (8), 1237–1251.